INTEGRATED CIRCUITS LABORATORY
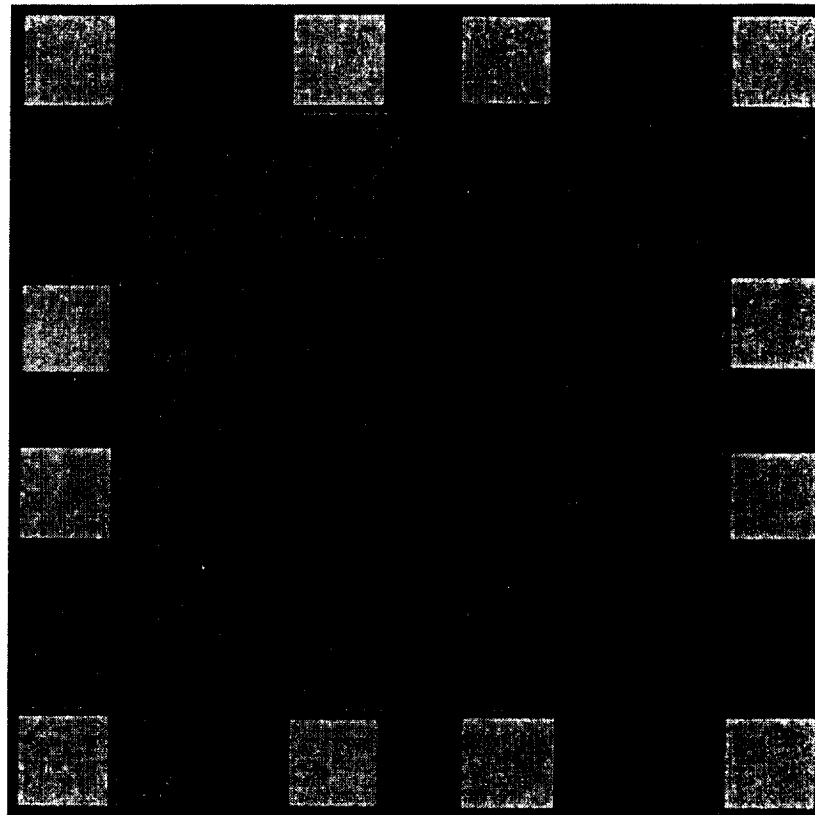
DEPARTMENT OF ELECTRICAL ENGINEERING

STANFORD UNIVERSITY • STANFORD, CA 94305

THE BIOLINK IMPLANTABLE
TELEMETRY SYSTEM

by Rafael J. Betancourt-Zamora

May 1999

E A R

Final Report

THIS PAGE INTENTIONALLY LEFT BLANK

TABLE OF CONTENTS

LIST OF FIGURES

LIST OF TABLES

THIS PAGE INTENTIONALLY LEFT BLANK

The BioLink Implantable Telemetry System

Executive Summary

Most biotelemetry applications deal with the moderated data rates of biological signals. Few people have studied the problem of transcutaneous data transmission at the rates required by NASA's Life Sciences-Advanced BioTelemetry System (LS-ABTS). Implanted telemetry eliminate the problems associated with wire breaking the skin, and permits experiments with awake and unrestrained subjects. Our goal is to build a low-power 174-216MHz RF transmitter suitable for short range biosensor and implantable use.

The BioLink Implantable Telemetry System (BITS) is composed of three major units: an Analog Data Module (ADM), a Telemetry Transmitter Module (TTM), and a Command Receiver Module (CRM). BioLink incorporates novel low-power techniques to implement a monolithic digital RF transmitter operating at 100kbps, using QPSK modulation in the 174-216MHz ISM band. As the ADM will be specific for each application, we focused on solving the problems associated with a monolithic implementation of the TTM and CRM, and this is the emphasis of this report.

A system architecture based on a Frequency-Locked Loop (FLL) Frequency Synthesizer is presented, and a novel differential frequency discriminator that eliminates the need for a frequency divider is also shown. A self-sizing phase modulation scheme suitable for low power implementation was also developed. A full system-level simulation of the FLL was performed and loop filter parameters were determined. The implantable antenna has been designed, simulated and constructed. An implant package compatible with the ABTS requirements is also being proposed.

Extensive work performed at 200MHz in 0.5µm CMOS showed the feasibility of integrating the RF transmitter circuits in a single chip. The Hajimiri phase noise model was used to optimize the VCO for minimum power consumption. Two test chips were fabricated in a 0.5µm, 3V CMOS process. Measured phase noise for a 1.5mW, 200MHz ring oscillator VCO is -80dBc/Hz at 100KHz offset, showing good agreement with the theory.

We also propose a novel superregenerative receiver architecture for implementing the command receiver. The superregenerative receiver's simplicity, low cost, and low power consumption has made it the receiver of choice for short-distance data communications, remote control and home automation We present the design of a super-regenerative AM receiver implemented in a 0.5µm CMOS technology that operates at 433.92MHz and dissipates only 300µW.

Further work entails detailed transistor-level design of the FLL and superregenerative receiver and a monolithic implementation of an implantable transceiver in 0.5µm CMOS technology.

1.0 Introduction

Currently, NASA-Ames Research Center is developing the Life Sciences-Advanced BioTelemetry System (LS-ABTS) to conduct space-based animal research [NASA95], [Hines95]. In vivo experiments require anesthetized animals and hard-wired connections to the implant creating a risk of infection due to transcutaneous wires. Wire breakage, movement artifacts, ground loops and 60Hz pick-up can also cause problems. NASA requires a low-power implantable transmitter that can relay biosensor data using an RF digital link in the VHF television band (174-216MHz). NASA is targeting 2.5KHz of total baseband signal bandwidth equivalent to 100kbps per implant. Command and control of the unit is achieved through a 433MHz downlink. This design is being pursued using commercially available components. A low-power highly integrated radio transmitter is key to the success of this project.

In collaboration with the Fetal Treatment Center at the University of California at San Francisco Medical Center, NASA is also developing a system for wireless telemetry of physiological parameters of fetuses for monitoring and identifying distress after pre-natal surgery [Bealer94], [NASA96]. An implant that will monitor heart rate, temperature, pH, and amniotic fluid pressure is required to operate in-utero for up to 3 months. This application creates an urgent need for a biotelemetry transmitter for chronic studies of implantable pH sensors. Current experiments cannot continue beyond 12 days because of wire breakage. BioLink can reduce the cost and extend the life of such a device.

2.0 System Architecture

Figure 1 shows the overall system architecture of a BioLink-based biotelemetry implant. The amplifer array, multiplexer, and analog to digital converter (ADC) form the Analog Data Module (ADM).

The Telemetry Module (TM) includes a data buffer, a low-power crystal-controlled frequency synthesizer, a quadrature phase shift keying (QPSK) modulator, and a differential loop antenna driver. Data is received from the ADM and a header and CRC block are added by the TM. On command, the RF carrier is modulated with the resulting bit stream using Differential-QPSK. An RF amplifier drives a small loop antenna to radiate the signal.

The Frequency synthesizer is implemented as a frequency-locked loop, using a 24MHz low-power crystal reference oscillator. This requires a small external crystal that does not have a major impact on the size of the implant. A novel switched capacitor differential frequency discriminator (SC-DFD) allows for the selection of the transmit frequency in 3MHz increments in the 174MHz to 216MHz range.

The most important parameter of an implanted biotelemetry system is power dissipation. Power dissipation and implant lifetime determine the size of the battery which ultimately determines the size of the implant. A significant portion of the power budget for any implantable telemetry system is allocated to the generation of the RF carrier. Given this need for small, low-power wireless devices for biotelemetry, a low-power, integrated frequency synthesizer is required.

Command Receiver Module

Control Logic

Super-regenerative Receiver

Analog Data Module

MUX → ADC

Amplifier Array

Telemetry Transmitter Module

QPSK Modulator

RF Amp

FIFO

I   Q

200MHz Frequency Synthesizer

Power & Control

+
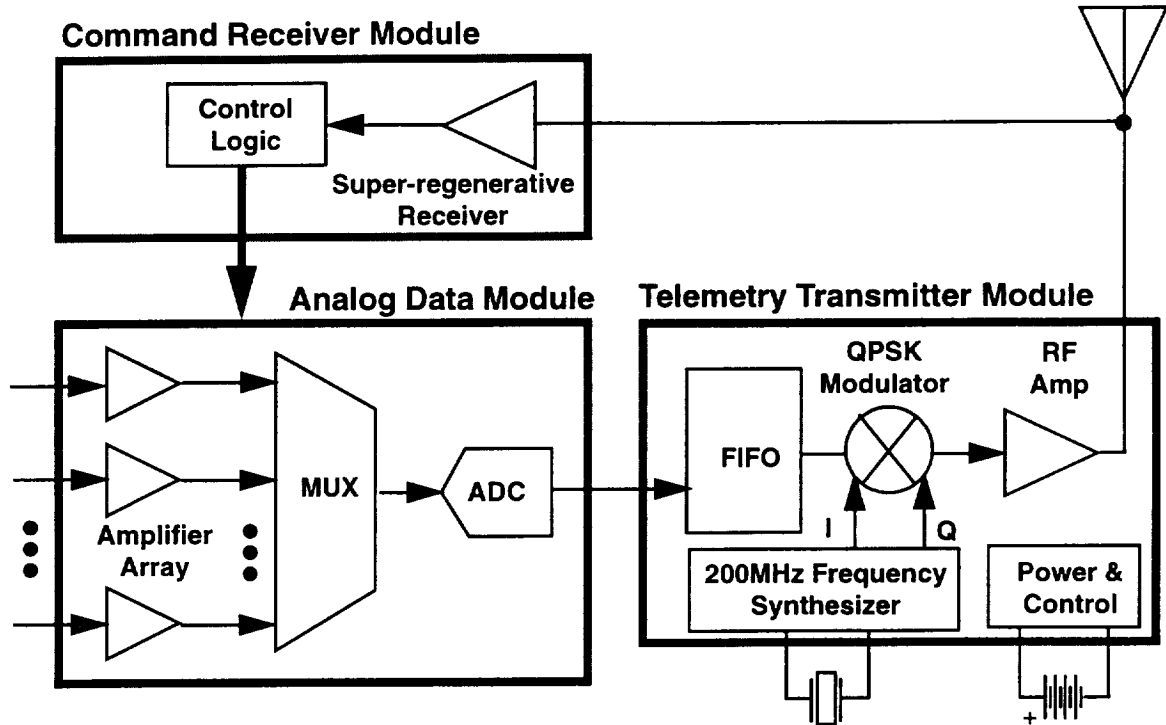
FIGURE 1. Overall system architecture of a BioLink-based biotelemetry implant

Traditionally, frequency synthesizers have been implemented using a phase-locked loop (PLL). Figure 2 shows the block diagram and power budget for a state-of-the-art CMOS PLL synthesizer used in microprocessor clock generation [vonKaenel96]. In a PLL synthesizer, the VCO frequency is divided and then compared to a reference frequency by a phase detector. The phase detector drives a low-pass filter that generate the control voltage for the VCO. The major sources of power dissipation are the VCO (73%) and the frequency divider (22%). To reduce power we have to address these blocks first.

We propose a frequency-locked loop (FLL) architecture (fig.3) that uses a switched capacitor differential frequency discriminator (DFD). In the past, quadricorrelators and rotational frequency detectors [Messerschmitt79] have been used to aid the frequency acquisition process in a PLL, but have been superseded by simpler phase-frequency detectors with charge pumps [Gardner80].

The Command Receiver Module (CRM) provides a mechanism to control remotely the power usage of an implant in order to extend its useful life. The inlink control channel can change the operating mode (Run, Standby, and Sleep), transmit frequency, and channel sampling rate. In the Run mode, the implant is fully operational. During Standby all high frequency circuits are disabled to save power. Sleep mode turns all systems off except for the receiver and low-frequency clock circuits. The BioLink inlink uses Manchester-encoded Amplitude Shift Keying (ASK) with a 433.92MHz carrier.
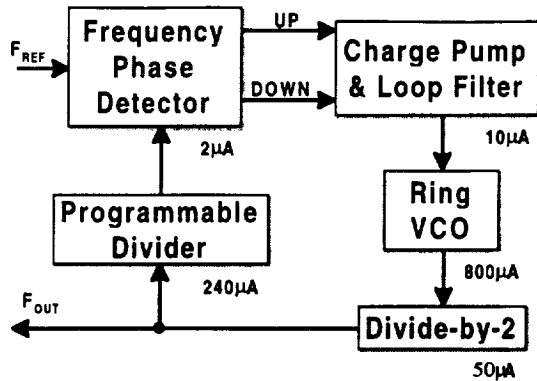
FIGURE 2. Power budget for a typical CMOS PLL frequency synthesizer used in microprocessor clock generation.
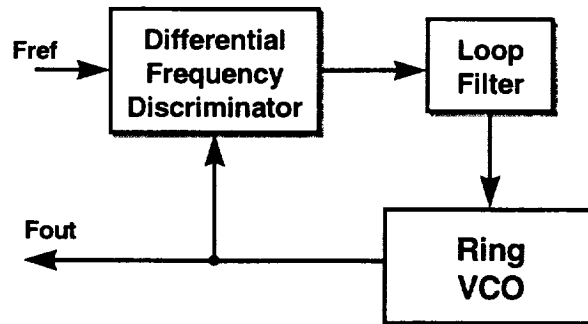
FIGURE 3. Frequency-locked loop (FLL) architecture that uses a differential frequency discriminator (DFD).

We propose a superregenerative receiver architecture for implementing the CRM. The superregenerative receiver, invented in 1922 by Armstrong [Armstrong22], was eventually supplanted by the superheterodyne receiver where high performance was required. Still, the superregenerative receiver's simplicity, low cost, and low power consumption has made it the receiver of choice for short-distance data communications, remote control and home automation. Recently, a 1.2mW, 1GHz superregenerative AM receiver was implemented by P. Farve, et al. in a 0.8µm BiCMOS technology [Farve98]. Its low power consumption, makes it very attractive for battery-powered applications. In this report, we present the design of a superregenerative AM receiver implemented in a 0.5µm CMOS technology that operates at 433.92MHz and dissipates only 300µW.

The FCC has authorized unlicensed use of the 38-41MHz, 88-108MHz, 174-216MHz and 433MHz bands for Industrial, Scientific and Medical (ISM) telemetry purposes [FCC15] (see Table 1). Other bands in the micro-wave region (900MHz and above) are not considered because of the high power required to operate at those frequencies. Ideally, the 40MHz band would be used as it is the lowest unlicensed band authorized by the FCC. The problem with this band is that only 3MHz are allocated making it difficult to accommodate applications requiring multiple transmitters in a group habitat. The 88-108MHz is usually very congested with FM commercial broadcasts, leaving only the 174-216MHz VHF television band available for biotelemetry. Up to 14 channels can be accomodated in this band, easing the selectivity and phase noise requirements of the system.

Frequency (MHz)	Bandwidth (KHz)	Field Strength (µV/m)	Out of band requirements (max.)
38-41	200	10 @ 15m	10µV/m @ 3m
88-108	200	50 @ 15m	40µV/m @ 3m
174-216	200	150 @ 30m	15µV/m @ 30m

TABLE 1. VHF Industrial, scientific, and medical (ISM) frequency allocation in the United States.

System	Zn/HgO	Zn/Ag$_2$O	Zinc/Air	Li/SOCl$_2$
Cell Voltage	1.35	1.5	1.5	3.65
Energy Density Gravimetric (Wh/kg)	100	120	340	480
Volumetric (Wh/L)	470	500	1050	950
Advantages	high energy density; flat discharge; stable voltage	high energy density; good high-rate performance	high energy density; long shelf life (sealed)	high energy density; long shelf life; flat discharge
Disadvantages	Low gravimetric energy density	Low gravimetric energy density	Not independent of environment	Very low discharge rate

TABLE 2. Comparison of primary battery technologies

3.0 Power Source

Power dissipation is the major limiting factor in the performance of a biotelemetry implant. In the past mercury (Zn/HgO) and silver (Zn/Ag$_2$O) oxide cells have been used [Mackay70] and more recently lithium cells [Owens86]. Table 2 show a comparison of the best performing primary battery technologies [Linden95]. Even though Zinc/Air technology offers very high energy density, it requires a source of oxygen, making it unsuitable for a sealed implant. Lithium thionyl chloride (Li/SOCl$_2$) batteries have the highest energy density (480Wh/kg) as well as high cell voltage and long shelf life.

Lithium thionyl chloride (Li/SOCl$_2$) cells have extremely long storage life (in excess of 10 years) but are capable of only low-rate discharge. Figure 4 shows the discharge characteristic of the Eagle-Picher LTC-7PN, (Li/SoCl$_2$) battery. It is rated at 750mAh, at 3.65V open circuit voltage. For a 2mA discharge rate, we get close to the expected lifetime of 375 hours, but at a 20mA drain it lasts for only 20 hours. This shows that very small currents can be drawn for long periods of time, but higher drain reduces significantly the useful life of the battery. The LTC-7PN has also been fully qualified by NASA for in-flight implantable biotelemetry.

The maximum current drain allowed, given the expected life of the implant is a critical issue for the design of a telemeter. Current drain limitations have to be considered when allocating the power budget of an implant. For instance, NASA's LS-ABTS requires 90 hours of implant lifespan for missions that will last up to 90 days. This constraints the maximum drain for the whole implant to about 5mA. For instance, a BioLink-based ABTS power budget could allocate up to 2mA for the TM 1mA for the CRM, and 2mA for ADM when operating at 100kbps using the LTC-7PN battery.

For these current drains, the battery might need preconditioning to avoid a prolonged turn-on voltage delay. The long shelf life of the Li/SOCl$_2$ cell is a result of the protective LiCl passivation film present on the anode. After storage, the cell may exhibit a delay in reaching its operating voltage because of the formation of this film. Once discharge is started, the passivation film is dissipated gradually, and the operating voltage is reached.
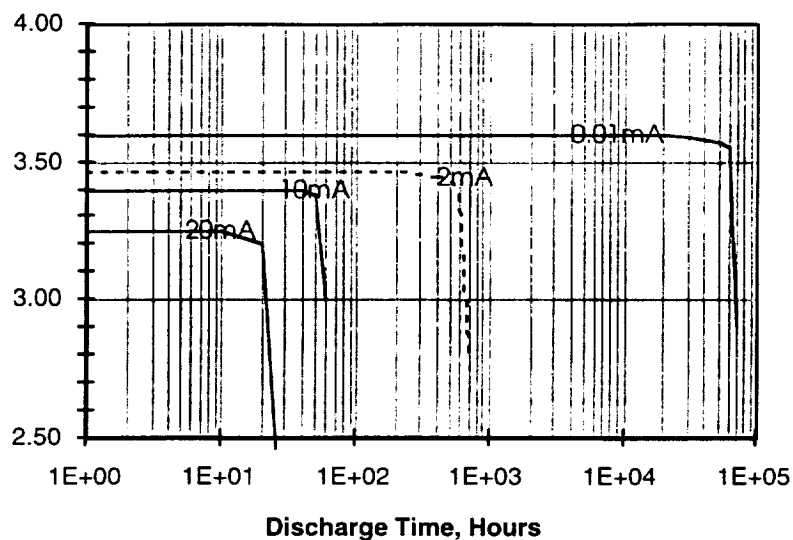
FIGURE 4. Eagle-Picher LTC-7P (Li/SOCl₂) discharge characteristic at 20°C

The passivation film in the LTC-7PN may be removed more rapidly by the application of high-current pulses for a short time period, or by preconditioning the cell with a 100kΩ load for a period of 64 hours. In a sealed implant, where the battery might be stored for six or more months, it is difficult to precondition the battery just before its use. Preconditioning is not necessary if the total standby current draw of the implant is about 35μA; this will prevent the passivation layer from forming, but will also reduce the available capacity by a small amount.

The size of the battery is also important, as it determines the minimum size of the implant. At 2.66cm³, and 6.8grams, the LTC-7PN is as large as can be practically accomodated in a rat implant (see Section 4.0 Packaging).

4.0 Packaging

The implant package must provide a moisture barrier to protect the electronics, and must not be toxic or harmful to the animal. Encapsulation in different kinds of epoxies as well as medical-grade silicone rubber (Silastic), and conformal coatings such as Parylene are well known. A major concern is sealing the I/O connections to the package. At Stanford, gold-plated Kovar packages with glass-to-metal feedthroughs were used extensively

[Knutti83] in the early 1980s, and systems were tested for more than two years using this type of package. In the past NASA has used machined ceramic packages for implanted telemeters. These are relatively large (7cm dia.), very expensive to manufacture, and are not readily available.

The package shoud be easy to implant, should cause minimum distress to the animal, and should maximize the efficiency of the RF system. Figure 5 shows a package concept that we believe meet these requirements [Jefferson96]. In BioLink the package not only protects the electronics, but also forms an integral part of the RF system. This package is implanted subcutaneously in the back of a rat.

Studies carried out at NASA using different size implants, showed that the preferred size should be less than $12.5cm^3$ (25 grams), for 300-400 grams rats [Somps95]. It was suggested by these studies that the form factor of the package can also affect the survival of the implant. A saddle package reduces the impact of the implant size on the animal by distributing the volume into two smaller saddle-bag pods. One pod contains the power source and the other the implant electronics. A flexible Kapton substrate joins the two modules and allows routing of signals and power, as well as provide an ideal location for the outlink antenna. The total volume of this implant, using the LTC-PN battery is $12cm^3$.
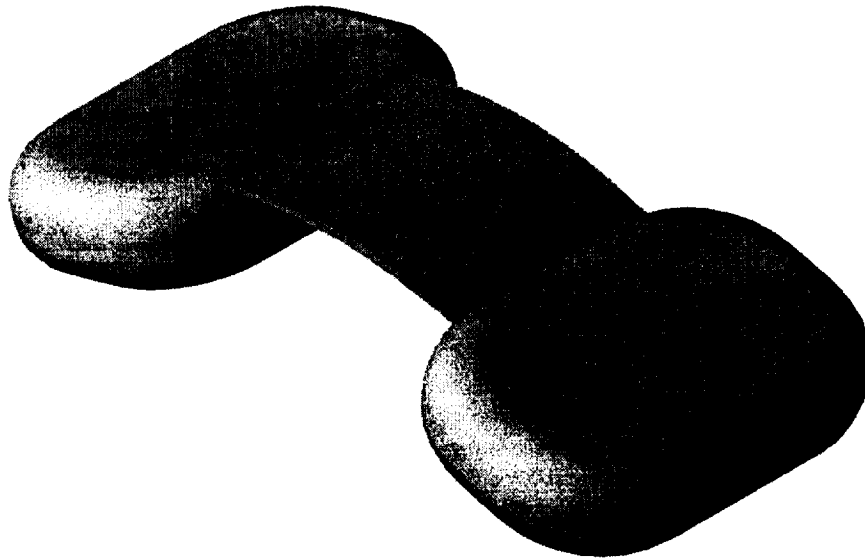
FIGURE 4. Saddle package with flexible antenna for rat implants

In this configuration the antenna placement minimizes the amount of tissue the signal has to go through, and the corresponding RF losses. Also, the flexible saddle allows for maximum loop area (see Section 5.0), which maximizes the signal coupling to the external antenna.

The BioLink implant electronics will be mounted directly to a 1 oz rolled-anealed copper-clad Kapton flexible substrate and conformally coated with Parylene. Fiberglass board stiffeners (FR-4) are used in the electronics pod to facilitate mounting of the components. This assembly is encased in a vacuum-formed medical-grade Ultem plastic enclosure, and coated with Silastic. The exposed Kapton belt in between the pods contain the outlink antenna as well as power leads from the battery. This belt also needs to be coated with Parylene and encapsulated in Silastic. A Dacron fabric mesh with suture hooks is added to the belt to ease implantation. This provides a very light and rugged encapsulation that protects the electronics as well as the animal.

5.0 Implantable Antenna Design[1]

Any radiating structure produces electrical and magnetic fields. A simple model of a wire carrying a varying current is described by:

$$E_r = \frac{i_0 L \cos\theta}{2\pi\varepsilon_0 c} \left\{ \frac{1}{d^2} + \frac{c}{j\omega_c d^3} \right\} e^{j\omega_c(t-d/c)}$$

$$E_\theta = \frac{i_0 L \sin\theta}{4\pi\varepsilon_0 c^2} \left\{ \frac{j\omega_c}{d} \frac{c}{d^2} + \frac{c^2}{j\omega_c d^3} \right\} e^{-j\omega_c(t-d/c)}$$

$$H_\phi = \frac{i_0 L \sin\theta}{4\pi c} \left\{ \frac{j\omega_c}{d} \frac{c}{d^2} \right\} e^{j\omega_c(t-d/c)}$$

In the above equations, all $1/d$ terms represent the radiation field component, all $1/d^2$ terms represent the induction field component, and all $1/d^3$ terms represent the electrostatic component. These equations describe two superimposed fields: a "near field" that starts off strong but falls off rapidly with distance, and a weaker "far field" that changes more slowly. The two become equal at distances from the transmitter of approximately $\lambda/6$. At distances a few times this, the electrostatic and inductive fleid components become negligible, and thus the far field becomes dominant. At a fraction of this distance, the near field is dominant, i.e., more power can be transferred through a near field at short distances than through the radiation field at large distances. At 200MHz, $\lambda=1.5$ meters, and thus the near field dominates inside a small cage, where the maximum transmission distance is well below 1 meter.
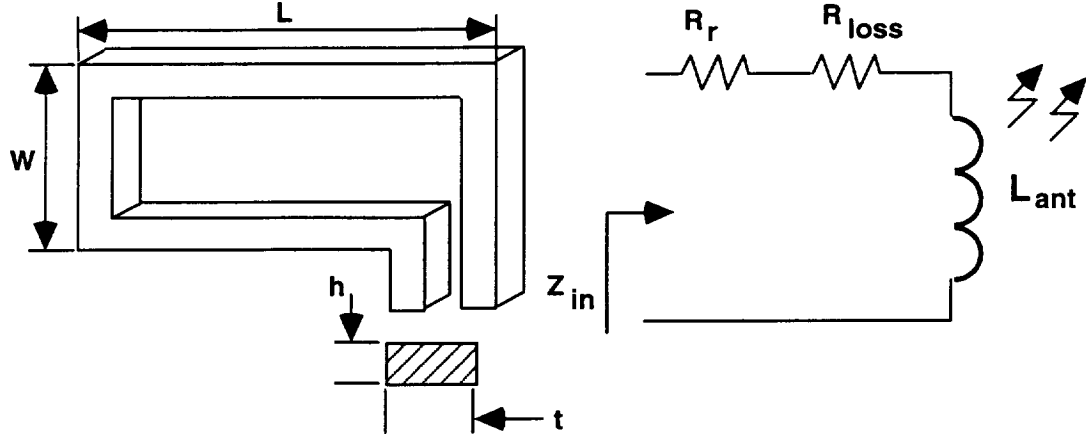
FIGURE 6. Single-turn loop antenna construction and electrical model

In the near-field region the main coupling mechanisms are electrostatic and inductive. Both dipole and loop antennas have been used in implanted applications [Mackay70]. Dipoles cannot be tuned as their $\lambda/4$ size (37.5cm @ 200MHz) is too large for implantation. Any electric dipole used will necessarily be electrically small. Inductive coupling is more efficient for near-field transmission inside a cage habitat, because the inductive terms $(1/d^2)$ fall off slower than the electrostatic term $(1/d^3)$.

The major drawback of wire loops is their sensitivity to misalignment with the receiving antenna. This is solved by using diversity reception where multiple antennas with different orientations are placed around the walls of a cage. For near-field coupling, the optimal receiving loop radius should be equal to the separation between the antennas [Terman50].

A single loop antenna with maximum area is usually the best choice for implanted telemeters [Mackay70]. Due to the voltage limitations imposed by the battery, the magnetic flux per volt is maximized using the least number of turns. Spreading the flux over a greater area also helps, and thus a single large turn is often the best antenna. To verify we performed an analysis of electrically small loop antennas [Fujimoto87],[Lau95].

The efficiency of the single loop antenna depicted in figure 6 is given by:

$$\eta = \frac{P_r}{P_s} = \frac{R_r}{R_r + R_{loss}} \qquad R_r = 20\left[\left(2\pi/\lambda\right)^2 A\right]^2$$

where Pr is the radiated power, Ps is the power form the source, Rr is the radiation resistance, Rloss is the loss resistance, and A= L x W is the loop area.

The loss resistance can be represented as:

$$R_{loss} = R_s L_{len} \Big/ L_{per} \quad \text{where} \quad R_s = \sqrt{\pi f \mu \Big/ \sigma} \quad L_{len} = 2(L + W) \quad L_{per} = 2(t + h)$$

where f is the frequency of operation, $\sigma = 5.813 \times 10^7$ S/m (conductivity of copper), and $\mu = 4p \times 10^{-7}$ A/m (permeability of copper), L and W are the length and width of the loop respectively.

We can extend this analysis to a multi-turn loop antenna, by defining the radiation resistance as:

$$R_{rN} = N^2 \times 20\left[\left(2\pi \Big/ \lambda\right)^2 A\right]^2 = N^2 \times R_r$$

where N is the number of turns.

The associated loss resistance is:

$$R_{lossN} = N \times \left(R_s L_{len} \Big/ L_{per}\right) = N \times R_{loss}$$

and the efficiency of the multi-turn loop is thus given by:

$$\eta = \frac{R_{rN}}{R_{rN} + R_{lossN}} = \frac{N^2 R_r}{N^2 R_r + N R_{loss}} \approx \frac{N R_r}{R_{loss}} \quad \text{for} \quad N R_{loss} >> N^2 R_r$$

This analysis neglects the proximity effect of closely space turns on the loss resistance. When two loops are placed close to each other, the proximity effect forces current to the outside edge of each conductor, increasing the loss resistance. To account for this non-uniform distribution of current along the loop, we redefine:

$$R_{lossNp} = N \times R_{loss}\left(1 + R_p \Big/ R_0\right)$$

where Rp is the resistance due to the proximity effect, R_0 is the skin-effect resistance per unit length and the ratio R_p/R_0 is a function of the spacing ratio (c/a, where 2c is the spacing between conductors and a is the equivalent wire radius) of the loops [Smith72]. By including the proximity effect on the efficiency calculation, we obtain:

$$\eta = \frac{N R_r}{R_{lossNp}} = \frac{N R_r}{R_{loss}\left(1 + R_p \Big/ R_0\right)}$$

The increase in efficiency with the number of turns is offset by the proximity effect. For two-turn loops the efficiency goes up typically by 2dB, but for three or more turns there is no longer a significant benefit.

The radiation resistance is calculated for the far-field, thus the results of this analysis are not completely applicable to the near-field case. In the near-field the ideas of transformer design are more relevant than the usual considerations of radio transmission. Still, this excercise provides some insights on how to maximize the performance of an antenna. This analysis shows that antenna efficiency increases with the loop area and number of turns, but at higher frequencies the skin effect limits the useful size of the loop and the proximity effect limits the number of turns to one or two.

To complete the antenna model we need to calculate the inductance of the loop, which is given by:

$$L_{ant} = \left(N^2 \frac{\mu_0}{\pi} \right) \times \left\{ L\ln\left[\frac{2A}{a}(L+L_c) \right] + W\ln\left[\frac{2A}{a}(W+L_c) \right] + 2[a + L_c - (L+W)] \right\}$$

$$L_c = \sqrt{W^2 + L^2}$$

and the quality factor of the loop can be calculated using:

$$Q_{ant} = \frac{j\omega L_{ant}}{R_r + R_{loss}} = \frac{f_r}{\beta}$$

where f_r is the resonant frequency and β is the antenna bandwidth. For operation at the 200MHz ISM band, the required Q is about 6.5.

The antenna impedance is given by:

$$Z_{in} = (R_r + R_{loss}) + j\omega L_{ant}$$

This impedance has to be matched to the transmitter in order to maximize the power transfer. The complete antenna circuit is shown in figure 7 where C_1 and C_2 form a matching network that transforms the input impedance and also resonates the antenna to the operating frequency given by:

$$f_r = \frac{1}{2\pi\sqrt{L_{ant}\left(\frac{C_1 C_2}{C_1 + C_2} \right)}}$$
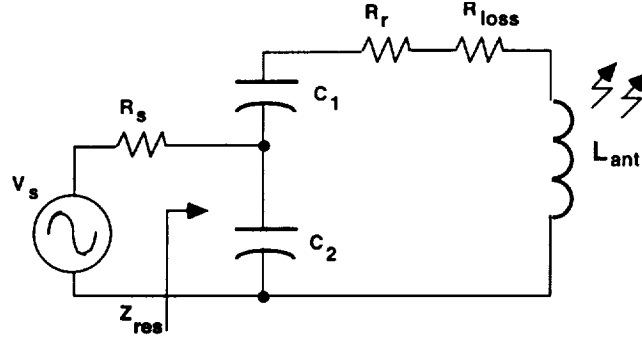
FIGURE 7. Equivalent circuit for small loop antenna

The loaded-Q, when the antenna is matched to the transmitter is given by:

$$Q_L = \frac{1}{2}Q_{ant} = \frac{\omega L_{ant}}{2(R_r + R_{loss})}$$

and at resonance, the impedance including the matching network is given by:

$$|Z_{res}| = \frac{L_{ant}}{(R_r + R_{loss})\left(\frac{C_1 C_2}{C_1 + C_2}\right)}\left(\frac{C_1}{C_1 + C_2}\right)^2$$

By proper selection of C1 and C2, the antenna can be tuned for 200MHz while allowing matching for maximum power transfer.

The BioLink outlink antenna is built in a flexible Kapton substrate, so our model have to account for the curvature of the loop. The reduction of the effective loop area affects both the radiation resistance and inductance. Assuming that the antenna is flexed along its width, the curvature correction factor is given by:

$$C_f = \frac{W'}{W} = \frac{\sqrt{2(1 - \cos\alpha)}}{\alpha}$$

where W' is the effective width for an angle α, and $0 < \alpha < 2\pi$.

A small (25 mm x 25mm) two-turn loop was built out of 1oz (h=34µm) copper-clad FR-4 (ε=4.8) rigid board material (1.6mm thick). This antenna was found to be self resonant at 195MHz. This design suffers from excessive parasitic capacitance, due to the construction of the loops with relatively large copper areas (to minimize Rloss) aligned in opposite sides of the board. Still, using a fixed 56pF chip capacitor in parallel with a high-Q tubular trimmer (0.6-4.5pF) we were able to tune the antenna to 40MHz. If we neglect the parasitic capacitance,
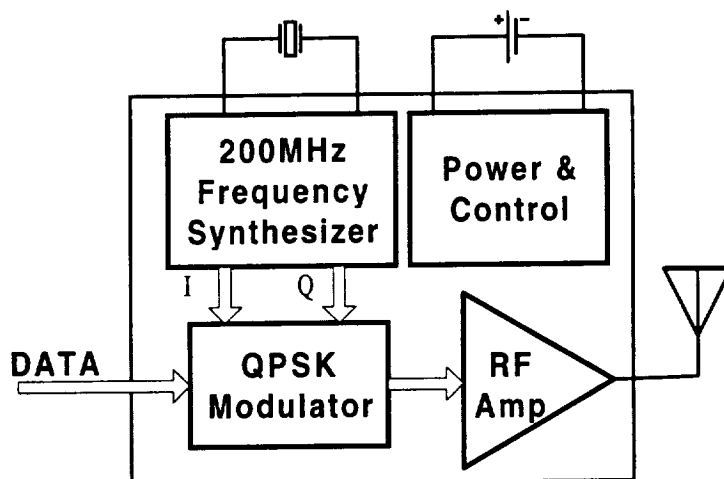
FIGURE 8. Telemetry Module Block Diagram

this corresponds to Lant=263nH, which is close to the theoretical value of 200nH. Radiation resistance for a loop this small is negligible, and the theoretical antenna efficiency approaches zero, thus the main mechanism for signal propagation is magnetic induction.

An experiment with a 2-turn loop (15mm x 20mm) of AWG.34 wire encapsulated in flexible Kapton tape carried out at 200MHz showed a difference of 2-8dB in power coupling when flexed with $\pi/2 < a < 2\pi/3$. Further experiments were carried out to characterize the performance of a flexible loop antenna at 200MHz. Results will be reported in a future paper.

6.0 Telemetry Transmitter Module

The Telemetry Transmitter Module (TTM) includes a data buffer, a crystal-controlled frequency synthesizer, a quadrature phase modulator, and a power amplifier (figure 8). A data packet is first assembled in a FIFO and a header and CRC block are added by the controller. On command, a packet is serialized and a 174-216MHz carrier is modulated with the resulting bit stream using differential quadrature phase shift keying (DQPSK). An RF power amplifier drives a small loop antenna to transmit the signal. The external RF circuitry is composed of the loop antenna and its matching network.

The Frequency synthesizer is implemented as a Frequency-Locked Loop, using a 24MHz low-power crystal reference oscillator. It generates both In-phase and Quadrature outputs necessary for QPSK modulation. A programmable differential frequency discriminator (DFD) allows for the selection of the transmit frequency in 3MHz increments in the 174MHz to 216MHz range.

Module	Subsystem	Imax (μA)
TTM	FLL Synthesizer & RF Amp	1000
	24 MHz crystal oscillator	105
	QPSK encoder/modulator	500
	Data Buffer	100
	ADM interface	200
	Control Logic	200
	Total TTM	2105

TABLE 3. Telemetry Transmitter Module Power Budget

As previously discussed the overriding concern in the design of an implant is power dissipation. Table 3 shows the preliminary power allocation for the TTM. This power budget is a constant and important reminder that architectural and implementation choices in any of the subsystems will have an impact on the others.

Following is a discussion of the encoding and modulation techniques considered for BioLink and the rationale behind the design decisions made.

6.1 Encoding Techniques

Baseband signals need to be encoded before modulation of the RF carrier. In Pulse Amplitude Modulation (PAM), a series of discrete samples from different analog sources are time-multiplexed into a single stream. Each sample is held for a time T, but its value is not quantized nor digitized. Synchronization pulses are usually added to the PAM stream [Ji92]. Previous work used the PAM stream to frequency modulate an 80MHz carrier directly [Dorman85]. Passive AM systems has also been reported [Slocum85] where a reflected impedance transmitter is used. These systems suffer from fading due to subject movement, usually have poor Signal to Noise Ratio, and only work well with restrained subjects.

Schemes where the signal voltage is encoded into pulses has also been used extensively. Pulse Width Modulation (PWM) has been used for low data rate transmission of physiological parameters [McCutcheon76], [Shapiro89]. In PWM each sample of a PAM stream is converted into a pulse with a duty cycle proportional to the sampled voltage. Pulse Position Modulation or Pulse Interval Modulation (PPM/PIM) is a variation of PWM where the information is conveyed in the time between two narrow pulses. In applications with very low data rates this technique achieves significant power savings by turning off the RF oscillator in the interval between the pulses. Power cycling does not work for modulation rates over a few kilohertz because it is very difficult to stabilize an RF oscillator within a fraction of a milisecond. Power cycling also generates spurious signals that can cause serious interference with neighboring transmitters.

Detailed analysis of PWM/PPM signals requires using a double Fourier series expansion in two variables, and is quite complex [Black53]. A simpler analysis is possible if we consider that a PWM/PPM system must be able to

resolve the minimum pulse width τ produced by the encoder. The spectrum of a periodic pulse sequence with amplitude Am, period T, and pulse width τ is given by

$$f(t) = \frac{2}{T} \sum_{n=1}^{\infty} |c_n| \cos(\omega_n t)$$

where

$$\omega_n = \frac{2\pi n}{T}$$

and

$$c_n = \tau A_m \frac{\sin\left(\omega_n \tau/2\right)}{\left(\omega_n \tau/2\right)}$$

for n = 1, 2, 3 ...

The spacing between harmonics is $2\pi/T$. As T decreases the harmonics move farther apart. As the pulse width τ decreases, the first zero crossing moves out in frequency. For τ << T most of the signal energy will lie in the range $0 < \omega_n < 2\pi/\tau$. The bandwidth (to the first zero crossing) is thus defined by

$$\omega = \frac{2\pi}{\tau}$$

For example, to transmit 25,000 8-bit samples per second using PWM would require

$$f = \frac{1}{\tau} = \frac{1}{T/2^8} = 25 \times 10^3 \times 256 = 6.4 MHz$$

These pulse techniques, even though adequate for low data rates, are impractical for signals above a few kilo-Hertz due to the excessive bandwidth required.

In Pulse Code Modulation (PCM), a PAM stream is quantized and digitized by an Analog to Digital converter (ADC). The resulting bit stream is further encoded and shaped to suit the synchronization and RF modulation methods used further downstream. Several PCM biotelemetry systems have been reported in the literature [Fryer74], [Leung86], [Cupal89].

Some advantages of PCM include greater noise immunity and robustness to channel impairments, easier multi-plexing of various channels, and ability to accomodate digital error-control codes. PCM also supports complex signal conditioning techniques such as source coding, encryption and equalization to improve the overall performance of the link. Due to its many advantages over analog encoding techniques, PCM encoding is the method of choice for BioLink.

Packet Field	Definition
1010 1010 1010 10	14-bit Preamble
11	2-bit Start of Frame Delimiter
RRRR BBBB	4-bit Rodent Identification Number 4-bit BioLink ID Number
CC SSSS SSSS • • •	2-bit Error Control Field 8-bit Sample Data Field (repeat for 8 channels)

TABLE 4. BioLink Outlink Packet Format

6.2 Communication Protocol and Synchronization

Synchronization is achieved by sending data as packets using a protocol similar to those proposed by M. Geisler [Geisler95], and the IEEE 802.3 standard. Each packet is made up of a header, data block, and error control block (Table 4).

The Header consists of a Packet Preamble (PP), Packet Type (PT), Rodent Identification Number (RID), and BioLink Identification Number (BID). The Packet Preamble allows the external receiver to detect the carrier and synchronize with the incoming packet. It consists of an alternating 1,0 pattern followed by the Start of Frame Delimiter (SFD) consisting of two consecutive 1's. The Type Field identifies the packet as being either Status or Data. The Rodent and BID numbers uniquely identify the implant. The CRM has a separate programmable register that holds the Packet Type, Rodent Number and BIN. These are automatically added to the packet during transmission.

The data block consists of 8 data words with 10 bits each. Each word has a 2-bit Error Control (EC) field and a 8-bit Data Field (DF). Data is received from the ADM into a buffer on the TTM, and when commanded, a header is attached, Checksum is generated, and the RF power circuits are energized to send the packet.

The EC field is a 16-bit Cyclic Redundancy Check (CRC) word calculated and appended to a packet during transmission. During reception, error-free packets result in a specific pattern in the CRC generator. Packets with improper CRC are rejected. Bit synchronization is implemented in the QPSK modulator and is an integral part of the Self-Synchronizing DQPSK modulation technique described in Section 6.3.6.

6.3 Modulation Techniques

Modulation theory provides insights on the basic tradeoff of transmitter power efficiency versus bandwidth efficiency. Modulation design is primarily concerned with the tradeoff of signal power versus error rate over a band-limited noisy channel. This provides an insight into saving transmitted signal power, which saves battery power and prolongs the lifetime of the implant. In Section 6.4.1, it is demonstrated that the transmitted power is just a fraction of the total power required by the transmitter to generate the RF carrier. Thus, the criteria for selecting a modulation scheme is based on maximizing the practical power efficiency which includes the biasing of the circuits used in its implementation. Following is a brief review of the modulation techniques available for biotelemetry and a comparison of their theoretical power efficiency.

6.3.1 Amplitude Shift Keying (ASK)

Is a special case of Amplitude Modulation where the binary values are represented by two different amplitudes of the carrier frequency can be described by:

$$f_c(t) = \begin{cases} A\cos(\omega_c t), & b = 1 \\ 0, & b = 0 \end{cases}$$

Taking the Fourier transform , we obtain:

$$F_c(\omega) = \frac{A}{2}\left[F(\omega - \omega_c) + F(\omega + \omega_c)\right]$$

The effect is to shift the spectrum of the baseband signal up to frequency ω_c with symmetrical sidebands around ω_c. The transmission bandwidth is twice the initial baseband bandwidth.

6.3.2 Frequency Shift Keying (FSK)

The carrier alternates between two frequencies, where ω_1 corresponds to a binary 1, and ω_2 to a binary 0, and can be described by

$$f_c(t) = \begin{cases} A\cos(\omega_1 t), & b = 1 \\ A\cos(\omega_2 t), & b = 0 \end{cases} \quad \text{, for} \quad -\frac{T}{2} \le t \le \frac{T}{2}$$

where T is the baseband pulse width. The frequency spectrum of FSK is difficult to obtain. A special case using a sequence of alternating 1's and 0's leads to a good rule of thumb for FM bandwidth and is much easier to evaluate [Schwartz80]. If the two frequencies are synchronized in phase and given by

$$f_1 = \frac{m}{T}, \text{ and } f_2 = \frac{n}{T},$$

---

where m,n are integer, then the spectrum is given by

$$\frac{\sin\left[(\omega_1 - \omega_n)\frac{T}{2}\right]}{(\omega_1 - \omega_n)\frac{T}{2}} + (-1)^n \frac{\sin\left[(\omega_2 - \omega_n)\frac{T}{2}\right]}{(\omega_2 - \omega_n)\frac{T}{2}}, \text{ where } \omega_n = \frac{\pi n}{T}$$

The spectrum can be visualized as two superimposed periodic ASK signals. The bandwidth (to first zero crossing) is then

$$B_t = 2B(1 + \beta)$$

where B is the baseband bandwidth. The parameter β is defined as

$$\beta = \frac{(f_1 - f_2)/2}{B} = \frac{\Delta f}{B}$$

where Δf is called the *frequency deviation*. This result is also known as Carson's rule. If $\Delta f \gg B$, the bandwidth approaches $2\Delta f$, and it is called *wideband* FM. The bandwidth is essentially independent of the baseband bandwidth. For $\Delta f \ll B$, the bandwidth approaches 2B, and is called *narrowband* FM. The bandwidth is essentially the same as for ASK, and is determined by the baseband signal. The minimum spacing required for noncoherent detection of FSK is 1/T Hertz.

It is the expansion of transmission bandwidth that increases the noise immunity, thus narrowband FSK does not have a SNR advantage over ASK. FSK's constant envelope has an advantage when transmitting through a nonlinear channel, and although implementing ASK is simple, it has relatively poor error performance and susceptibility to fading and nonlinearities [Smith93].

6.3.3 Binary Phase Shift Keying (BPSK)

The phase of a constant amplitude carrier is switched between two values corresponding to binary 1 and binary 0 respectively. The two phases are separated by 180 degrees, and can be described by

$$f_c(t) = m(t)\cos\omega_c t, \text{for } -\frac{T}{2} \leq t \leq \frac{T}{2},$$

where T is the baseband pulse width, and $m(t)$ has values of +1 for a binary 1, and -1 for a binary 0. BPSK is equivalent to a double-sideband suppressed carrier amplitude modulation, where $\cos\omega_c t$ is the carrier and $m(t)$ is the modulating signal. It has the same double-sideband characteristic as ASK, where the bandwidth is twice that of the baseband signal, centered at the carrier f_c.
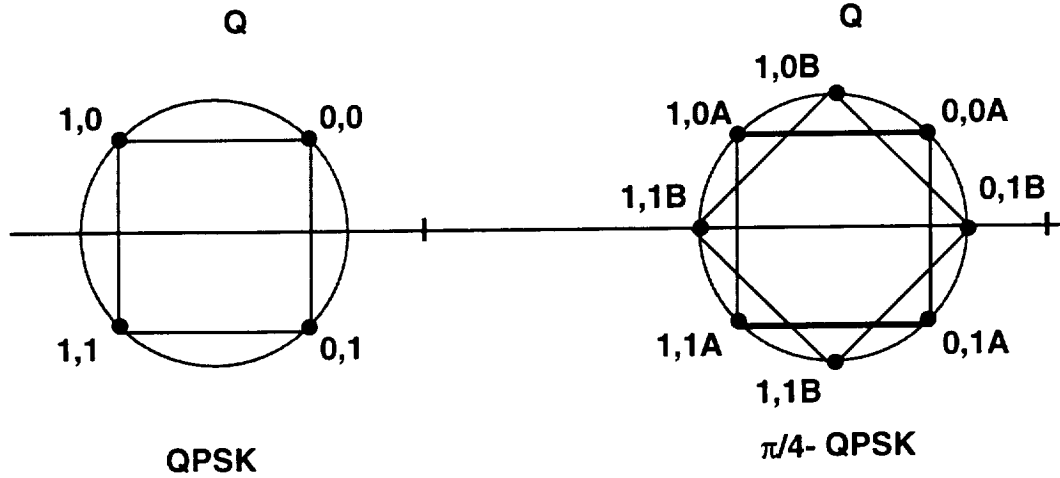
FIGURE 9. QPSK and π/4-QPSK constellation diagram.

Differential BPSK (DBPSK) is a noncoherent form of PSK which avoids the need for a phase-coherent reference at the receiver. The input signal is first differentially encoded and then modulated using BPSK. While DBPSK signaling has the advantage of reduced receiver complexity, its energy efficiency is inferior to that of coherent BPSK by about 1dB.

6.3.4 Quadrature Phase Shift Keying- (QPSK)

The phase of the carrier takes on 1 of 4 equally spaced values (π/4, 3π/4, 5π/4, 7π/4), where each phase corresponds to a unique pair of message bits (figure 9). QPSK has twice the bandwidth efficiency of BPSK, since 2 bits are transmitted as a single modulation symbol. The QPSK signal for this set of symbols may be defined as

$$f(t) = \sqrt{\frac{2E_s}{T_s}} \cos\left[2\pi f_c t + (i-1)\frac{\pi}{2}\right], \text{where } 0 \le t \le T_s, \text{ and } i = 1, 2, 3, 4.$$

where T_s is the symbol duration and is equal to twice the bit period. The bit error probability of QPSK is identical to BPSK, but twice as much data can be sent in the same bandwidth, i.e., QPSK provides twice the spectral efficiency with exactly the same energy efficiency.

6.3.5 Modulation Tradeoffs: Power, Noise and Bandwidth

Modulation design is primarily concerned with maximizing the bandwidth efficiency, and minimizing the power required for transmission while maintaining an acceptable bit error rate (BER). The most important parameter in determining the performance of a digital communication system is the signal to noise ratio (SNR). SNR is defined by

$$(S/N)_{dB} = 10 \log \frac{S_{power}}{N_{power}}$$

which is the ratio of signal power to noise power in a given bandwidth.

Shannon showed that the theoretical maximum channel capacity, in bits per second (bps) is given by

$$C = B \ log_2 \left(1 + S/N \right)$$

where B is the channel bandwidth in Hertz [Shannon49]. In practice, however, only much lower rates are achievable, as this formula only accounts for thermal noise. It can be seen how the SNR determines the upper bound on the achievable data rate.
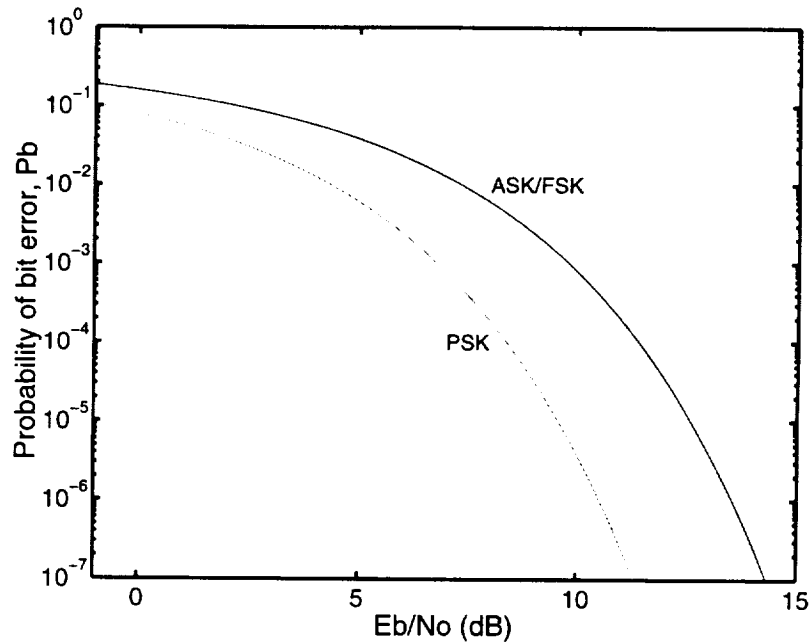

FIGURE 10. Probability of Error vs. E_b/N_0 for ASK, FSK, and PSK modulation schemes.

Modulation	Bandwidth (200kbits/sec)	BW Efficiency, R/B (bits/Hz)	E_b/N_0 (BER=10^{-6})
ASK	400KHz	0.5	13.5dB
FSK	400KHz	0.5	13.5dB
BPSK	400KHz	0.5	10.5dB
QPSK	200KHz	1.0	10.5dB

TABLE 5. Comparison of various digital modulation schemes

A parameter related to SNR is the ratio of signal energy per bit to noise energy per Hertz, E_b/N_0. This ratio is defined as

$$E_b/N_o = \frac{(S/N)}{(R/B)}$$

where R is the bit rate, and the ratio (R/B) is the bandwidth efficiency. E_b/N_0 is important because the bit error rate (BER) is a decreasing function of this ratio. As the bit rate R increases, the transmitted signal power, relative to noise, must increase to maintain the required E_b/N_0.

Figure 10 shows the probability of bit error P_e versus E_b/N_0 for ASK, FSK, BPSK and QSK modulation schemes, assuming coherent detection. As E_b/N_0 increases, the error rate drops. For P_e less than 10^{-5}, BPSK/QPSK show a 3dB advantage in SNR over ASK/FSK.

Table 5 compares ASK, FSK, BPSK and QPSK modulation methods for a 200kbps data rate and BER=10^{-6}. ASK and FSK have the same E_b/N_0 performance as well as the same bandwidth efficiency. Both BPSK and QPSK have a 3dB advantage over ASK/FSK, and QPSK is clearly superior with twice the bandwidth efficiency of BPSK.

Encoding	Analog Modulation		Digital Modulation			
	AM	FM	ASK	FSK	BPSK	QPSK
PAM	[Slocum85]	[Dorman85]				
FM		[Jeutter83]				
PPM	[Henry92]					
PCM			[Hines95]	[Jeutter95]	[Fernald92]	BioLink

TABLE 6. Reported Biotelemetry Encoding and Modulation Alternatives

The transmitted signal power represents just a fraction of the total power required by the TTM. The choice of a modulation scheme should maximize the power efficiency accounting for the power allocation to other subsystems within the TTM. For instance, a QPSK modulator represents only 6.2% of the total power budget. Assuming that a simpler ASK/FSK modulator that dissipates no power is used instead, this would represent savings of only 0.28dB of the TTM budget. Thus, the choice of a modulator is strongly influenced by ease of implementation, and maximum SNR, not as much by theoretical power efficiency of the modulation scheme used.

BioLink use of Differential-QPSK is described in the next section. Table 6 shows how BioLink fits within the design space of encoding and modulation techniques reported in the implantable biotelemetry literature. BioLink is the first implantable biotelemetry system to use PCM/QPSK.

6.3.6 Self-Synchronizing Differential QPSK

The Self-Synchronizing Differential QPSK (SS-DQPSK) modulation scheme[2] combines data encoding and carrier phase modulation in one operation. This simplifies the hardware required for the modulator and reduces power dissipation.

To understand SS-DQPSK, it is useful to study the $\pi/4$-DQPSK modulation scheme used by the U.S. Digital Cellular system (EIA IS-54 standard). In a $\pi/4$-DQPSK modulator, signaling points are selected from two orthogonal QPSK constellations (figure 9). Switching between the two constellations every succesive bit ensures that there is at least a phase shift which is an integer multiple of $\pi/4$ between succesive symbols. This ensures that there is a phase transition for every symbol, which enables a receiver to perform timing recovery and synchronization.

BioLink scales the $\pi/4$-DQPSK scheme to a level more appropriate for low-power biotelemetry using two constellations with two signaling elements each, for a total of 4 phases. In SS-DQPSK, a binary 1 is transmitted as a $+\pi/2$ phase shift, and a binary 0 is represented by a $-\pi/2$ phase shift, thus ensuring a phase transition on every symbol. This scheme solves the problem of bit synchronization, as the bit clock is encoded in the phase shift. The encoder can be implemented with a simple 2-bit up/down counter, which uses very little power. The SS-DQPSK modulator essentially combines a DQPSK modulator with a bi-phase differential data encoder.

Differential encoding reduces the power efficiency by 1dB, but eliminates the problem of phase synchronization at the receiver. Power is saved transmitting packets in short bursts, by minimizing the time required by the receiver to acquire carrier lock. Bandwidth efficiency is reduced in half, because of the signal clock encoding, but this allows for a very robust and simple synchronization mechanism. Bandwidth efficiency of other modulation schemes would also be reduced in half if the signal is bi-phase (Manchester) encoded before modulation.

---

2. Also known as symmetric-QPSK [Hickman93].

6.4 RF Transmitter Design

BioLink uses an integrated class-C power amplifier to drive the antenna. The external RF circuitry is composed of a loop antenna and its matching network. This section discusses the selection of the operating frequency, spectrum allocation, link budget, and implementation issues of the RF power amplifier.

6.4.1 RF Spectrum Allocation

The most important issue of an implanted biotelemetry system is power dissipation. While VLSI circuits can help reduce the size of the implant, power dissipation and expected implant lifetime determine the size of the battery which ultimately determines the size of the implant. To minimize the power of a transmitter, we have to select the lowest practical RF carrier frequency, as RF circuits dissipate power that is proportional to their operating frequency.

The FCC has authorized unlicense use of the 38-41MHz, 88-108MHz, and 174-216MHz Very High Frequency (VHF) bands for Industrial, Scientific and Medical (ISM) telemetry purposes [FCC15]. Other bands in the microwave region (900MHz and above) are not considered because of the high power required to operate at those frequencies. As shown in Table 1, regulations limit the allowable RF field strength to minimize the interference with other authorized broadcasts. A major concern is also the effect on tissue of a strong RF field. To avoid tissue damage due to RF heating, the maximum RF power density should not exceed $10mW/cm^2$ [Neukomm76] . These constraints are not difficult to meet given that the required transmitted power is in the order of microWatts for experiments with caged small-animals.

Ideally, the 40MHz band would be used as it is the lowest unlicensed band authorized by the FCC. The problem with this band is that only 3MHz are allocated making it difficult to accomodate the high data rates required by neural signal telemetry. This is also unsuitable for low-rate applications requiring multiple transmitters in a group habitat. The 88-108MHz is usually very congested with FM commercial broadcasts, leaving only the 174-216MHz VHF television band available for biotelemetry. Up to 14 neural-grade channels can be accomodated in this band, easing the selectivity and phase noise requirements of the system.

In the BioLink system, the 174-216MHz ISM band is divided into 14 channel slots, each 3MHz apart. Every other slot is occupied, providing up to 7 simultaneous channels for a frequency-division multiple-access (FDMA) scheme. Having 3MHz of spacing between channels relaxes the requirements on the transmitter's phase noise and the external receiver's selectivity.

6.4.2 Link Budget and Transmitter Power

A first order analysis can be performed to determine the power required for the transmitted RF signal. The transmitter power P_t is given by

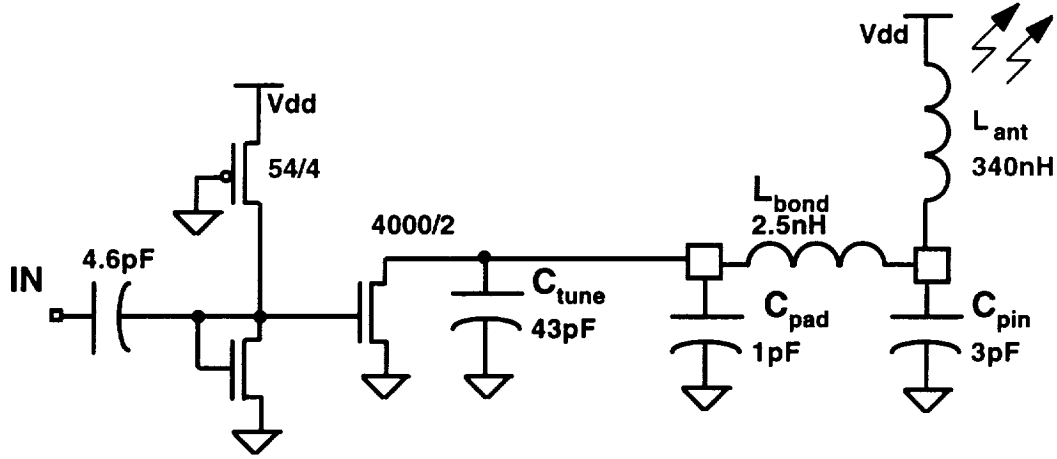$$P_t = L_p + kTo + 10\log R + N_f + \frac{E_b}{N_o}$$

FIGURE 11. Class-C RF Output Stage

where L_p is the transmission loss through tissue and air, kTo is -172.6dBm/Hz at body temperature (37°C), R is the data rate, and N_f is the receiver's noise. If we assume that N_f is 7dB, and L_p is 75dB [Fotowat84] for a data rate of 200kbps using QPSK modulation with a desired BER of 10^{-6}, then

$$P_t = 75 - 172.6 + 10\log(200x10^3) + 7 + 10.5 = -21.1 dBm = 7.7\mu W$$

This analysis gives a lower bound on the RF power output of the transmitter. In contrast, the BioLink VCO uses about 1.5mW to generate a 200MHz carrier. This clearly shows that the biasing requirements of the transmitter circuit, more than the actual power radiated, determine the power drain of the implant.

6.4.2 RF Power Amplifier

The basic trade-off is between power and range for a given SNR. An active transmitter, where an implanted RF source is used is the most common solution [Knutti83]. Active AM transmitters require a Class-A or Class-AB output stage (50-75% efficiency) due to linearity requirements [Hardy79]. These are not as efficient as the class-C amplifiers (up to 90% efficiency) usually used with FM transmitters. Performance is also affected by loading of biological materials on the antenna which can "pull" the frequency of the RF oscillator [Dorman85]. Using a buffered class-C output (figure 11), BioLink does not suffer from frequency "pull."
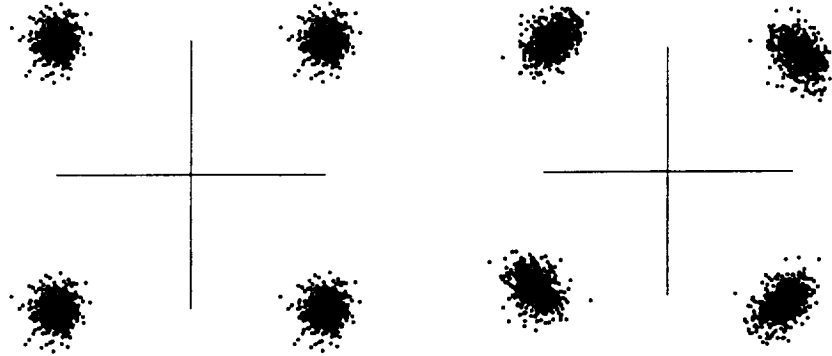
FIGURE 12. QPKS constellation: (a) with AWGN, (b) with AWGN and oscillator phase noise

6.5 Frequency Synthesizer Design

Frequency synthesizers provide the precise reference frequencies for modulation and demodulation of RF signals. All practical frequency sources have undesirable phase fluctuations due to intrinsic device noise. Phase noise is particularly important in RF systems as it can lead to (1) increased bit error rates (BERs) in digital communication systems, (2) contamination of adjacent frequency channels and (3) receiver desensitization due to reciprocal mixing where out-of-band signals are translated into the IF [Crawford94].

In a typical digital communication system, phase noise in the local oscillator can cause the signal constellation to rotate in a random fashion, thereby degrading the BER performance. As an example, Figure 12 shows the effects of noise on the constellation for a QPSK modulated signal, where (a) shows the effect of additive white gaussian noise (AWGN), while (b) adds the effect of phase noise at the carrier frequency. The noise have been exaggerated for illustration purposes. It shows how phase noise increases the probability of error in the detection of the signal by skewing the constellation thus reducing the effective distance between the symbols.

Traditionally, frequency synthesizers have been implemented using a phase-locked loop (PLL). Figure 2 shows the block diagram and power budget for a state-of-the-art CMOS PLL synthesizer used in microprocessor clock generation [vonKaenel96]. In a PLL synthesizer, the VCO frequency is divided and then compared to a reference frequency by a phase detector. The phase detector drives a low-pass filter that generate the control voltage for the VCO. The major sources of power dissipation are the VCO (73%) and the frequency divider (22%). To reduce power we have to address these blocks first. An alternative frequency-locked loop (FLL) synthesizer architecture has been proposed [Betancourt97], that eliminates the need for a frequency divider. A block diagram of the synthesizer is shown in figure 13.

A FLL synchronizes a voltage controlled oscillator (VCO) with a reference signal in frequency. In the synchronized state the frequency difference between the VCO's output and the reference is ideally zero. If a frequency error builds up, a feedback mechanism acts on the VCO to reduce the frequency difference. The frequency of the
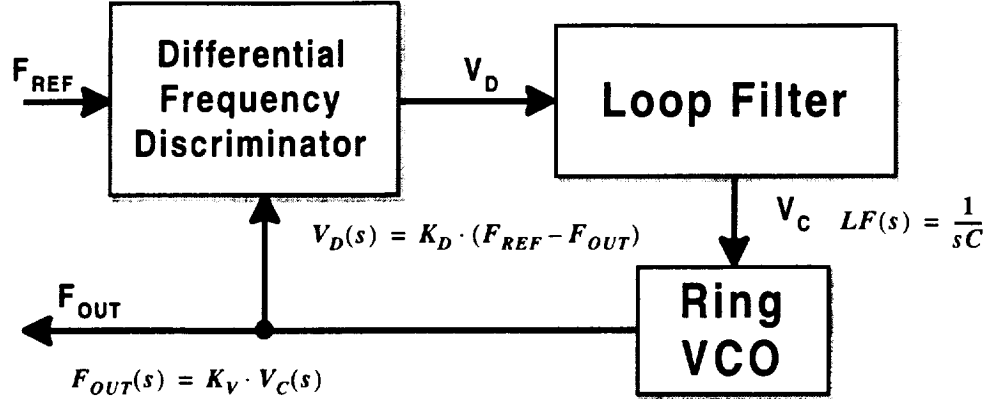
FIGURE 13. Block Diagram of the Frequency-Locked Loop Synthesizer

VCO is thus synchronized or locked with the frequency of the reference signal, and that is why this is called a Frequency-Locked Loop.

We propose a frequency-locked loop (FLL) architecture that uses the differential frequency discriminator (DFD) shown in figure 14. In the past, quadricorrelators and rotational frequency detectors [Messerschmitt79] have been used to aid the frequency acquisition process in a PLL, but have been superseded by simpler phase-frequency detectors with charge pumps [Gardner80] that require frequency dividers in the loop. The proposed FLL does not require a frequency divider, which represents 22% of the power budget for the PLL example just shown. The FLL can perform frequency comparison directly without a divider (N=1) by using a DFD implemented with switched capacitor circuits.

BioLink synthesizes the 174-216MHz RF carrier from a low-power 24MHz crystal oscillator using a frequency-locked loop (FLL). In BioLink, quadrature carriers are generated by a differential ring oscillator VCO. A switched capacitor differential frequency discriminator (DFD) compares the crystal reference to a scaled down version of the VCO frequency. The output of the DFD is filtered by a simple 1-pole filter, $1/sC$. The filtered output controls the biasing of the VCO, thus closing the loop. For a 0.5μm CMOS process, the VCO and crystal oscillator, use 500μA, and 100μA respectively at 3V. The whole synthesizer consumes about 600μA.

6.5.1 FLL Frequency Synthesizer Model

The closed-loop signal diagram for the FLL is shown in figure 13, and its phase transfer function is given by

$$\frac{F_{OUT}}{F_{REF}}(s) = \frac{1}{1 + s/\omega_N} \quad \text{where} \quad \omega_N = \frac{K_V \cdot K_D}{C}$$
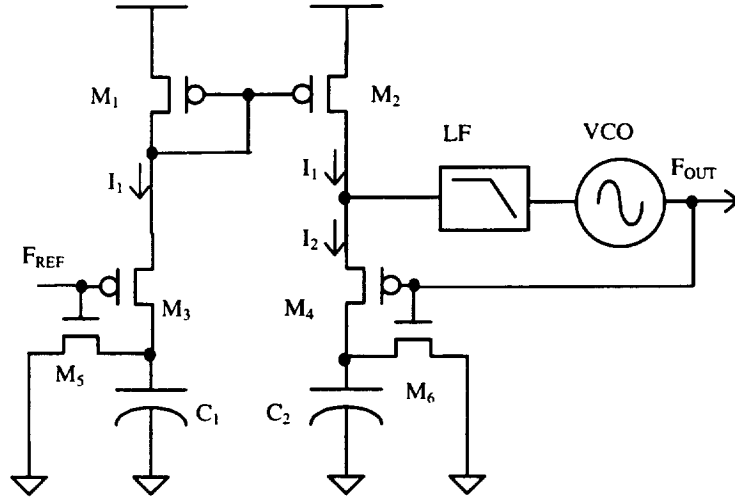
FIGURE 14. FLL Synthesizer uses a Differential Frequency Discriminator.

This function describes a first order system with one pole, where, K_V is the frequency to voltage transfer characteristic of the VCO, and K_D is the capacitor ratio of the DFD. A linear analysis shows that this system is inherently stable (neglecting sample-data effects).

6.5.2 Switched Capacitor Differential Frequency Discriminator Design

The differential frequency discriminator (DFD) is shown in figure 14. In operation, current I_1 is generated by switches S_1, S_2 and capacitor C_1, and is inversely proportional to the reference frequency driving the switches, F_{REF}, and the value of C_1. Current I_2 is also inversely proportional to the feedback frequency, and the value of C_2. Current mirror M_1/M_2 force these two currents to be equal, resulting in the following relationship:

$$F_{out} = \frac{C_1}{C_2} \cdot F_{ref}$$

where the output frequency is determined solely by the capacitor ratio, C_1/C_2.

6.5.3 Voltage-Controlled Oscillator Design

The VCO's power dissipation is determined by the frequency of operation and the phase noise performance required. Power dissipation at a given frequency cannot be made arbitrarily small, as it is constrained by the choice of technology, and by the system's phase noise requirements. VCO design is critical in the performance of the synthesizer, as the phase noise at the output of the FLL is solely a function of the phase noise of the VCO. This section presents a design methodology for differential ring oscillators suitable for FLL frequency synthesis,
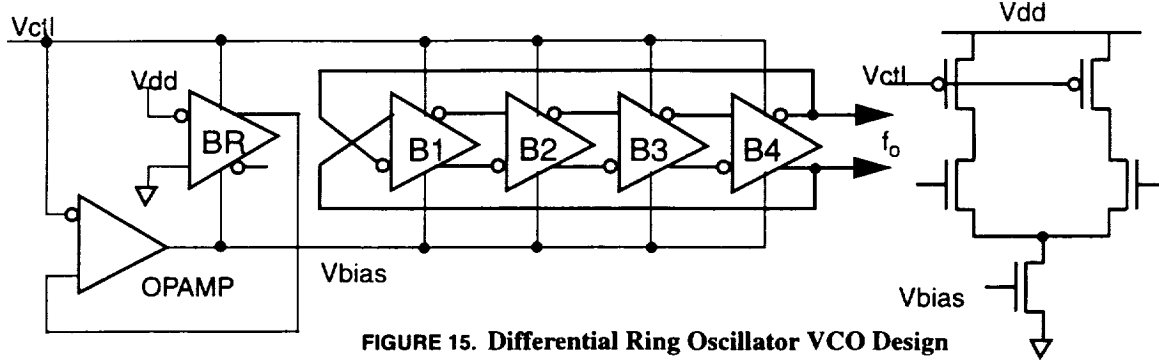
FIGURE 15. Differential Ring Oscillator VCO Design

that trades off power dissipation with phase noise. This methodology uses a new phase noise model to trade-off phase noise and power dissipation in the design of ring oscillators. We compare the theoretical phase noise performance of three buffer stages using clamped, symmetric and cross-coupled loads, respectively. We propose a cross-coupled buffer topology that achieves lower phase noise by exploiting symmetry. This achieved a 95% reduction in the $1/f^3$ corner frequency of the phase noise characteristic.

Selection Criteria for Oscillator Topology

In general, higher Q oscillators posses lower phase noise. Crystal oscillators have excellent phase noise characteristics, but are not suitable for tunable oscillators. Resonant LC oscillator also have very good phase noise performance, but require inductors that are difficult to implement in monolithic form. Monolithic inductors at 200MHz require large die areas and suffer from low Qs, which makes them unpractical for integration. Ring oscillators are often used as VCOs in monolithic PLL implementations. The ring oscillator has the worst phase noise performance of all VCO alternatives, but it is easy to integrate, and can run at very high frequencies with low power dissipation. In biotelemetry, data rates are low, and channel spacing wide, relaxing the phase noise requirements. This makes it feasible to use voltage-controlled ring oscillators which are easy to integrate and do not require any external components.

Power vs. Frequency Trade-off

For a differential ring oscillator, the total power dissipation is given by

$$P = NI_{dd}V_{dd}$$

where N is the number of stages, I_{dd} is the tail current of the differential pair, and V_{dd} is the supply voltage. The frequency of oscillation can be approximated by

$$f \approx \frac{I_{dd}}{2NC_LV_S}$$

where C_L is the load capacitance and V_S is the maximum single-ended voltage swing at the output of each stage.
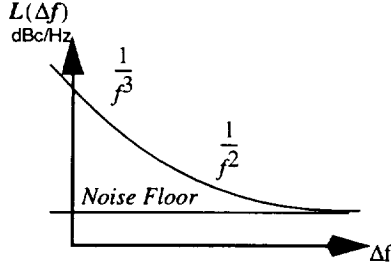
FIGURE 16. Oscillator Close-in Phase Noise due to upconversion of thermal and *1/f* device noise
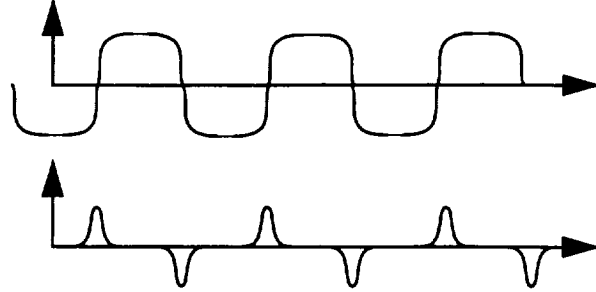

FIGURE 17. Ring oscillator waveforms: (a) single-ended output , $V_{out}(t)$, (b) inpulse sensitivity function $\Gamma(\omega t)$

The VCO consists of a 4-stage ring oscillator (Figure 15) that uses buffer delay stages with replica-feedback biasing [Maneatis93]. The buffers are NMOS differential pairs with linear PMOS loads. The replica bias feedback ensures that the loads are always in their linear region by forcing the swing V_s to be the same as $(V_{dd}-V_{ctl})$. Frequency control is achieved by varying V_{ctl} which also changes the bias I_{dd} of the buffer stages. The layout of the ring oscillator is symmetrical and load balanced to avoid any skewing between the phases.

Power vs. Phase Noise Trade-off

Phase noise performance of a synthesizer is a function of the phase noise of the VCO. The Hajimiri phase noise model [Hajimiri98a-c] predicts the upconversion of thermal and *1/f* device noise into close-in phase noise. Phase noise in the $1/f^2$ region is due to white device thermal noise (figure 16). For a differential ring oscillator using short-channel devices, one may derive the following lower bound on the single-sideband phase noise in the $1/f^2$ region:

$$L\{\Delta f\} \geq \frac{18kTV_{dd}}{\pi^2 P} \cdot \left(\frac{2.5}{E_C L_{eff}} + 1\right) \cdot \left(\frac{f_o}{\Delta f}\right)^2 \cdot N$$

where P is the power dissipation, E_C is the critical field in silicon, and L_{eff} is the gate length of the differential-pair devices. Observe that phase noise is a strong function of the number of stages, which justifies the selection of a 4-stage oscillator.

Phase noise in the $1/f^3$ region is due to device $1/f$ noise. It is usually assumed that the $1/f^3$ corner frequency is the same as the $1/f$ corner of device noise. This is not true, as the $1/f^3$ corner is actually given by:

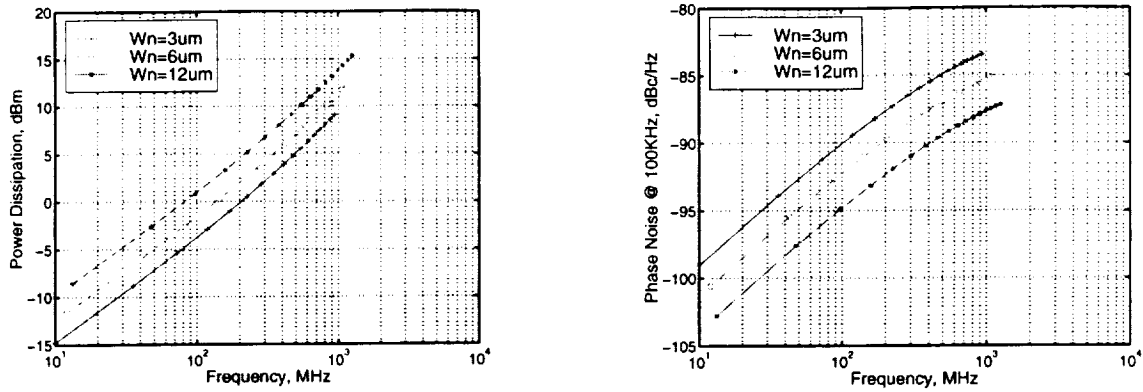$$f_{1/f^3} = f_{1/f} \cdot \frac{\Gamma_{dc}^2}{\Gamma_{rms}^2}$$

FIGURE 18. Power dissipation and phase noise for differential ring oscillator using PMOS linear loads and replica-feedback biasing: (+)Wn=3μm, (o)Wn=6μm, (*)Wn=12μm

where Γ_{dc} is the DC value and Γ_{rms} is the RMS value of $\Gamma(x)$, the impulse sensitivity function (ISF). The ISF is a function of the output waveform and it accounts for the time-variant sensitivity of the oscillator to its noise sources. Figure 17 shows the ISF corresponding to a typical ring oscillator waveform. We can observe a high sensitivity to noise at the transitions of the output waveform.

The upconversion of device $1/f$ noise occurs through Γ_{dc}. However, the DC value of the ISF is governed by the symmetry properties of the single-ended output waveform. This model thus predicts the upconversion of $1/f$ device noise into close-in phase noise as a function of the symmetry of the output waveform.
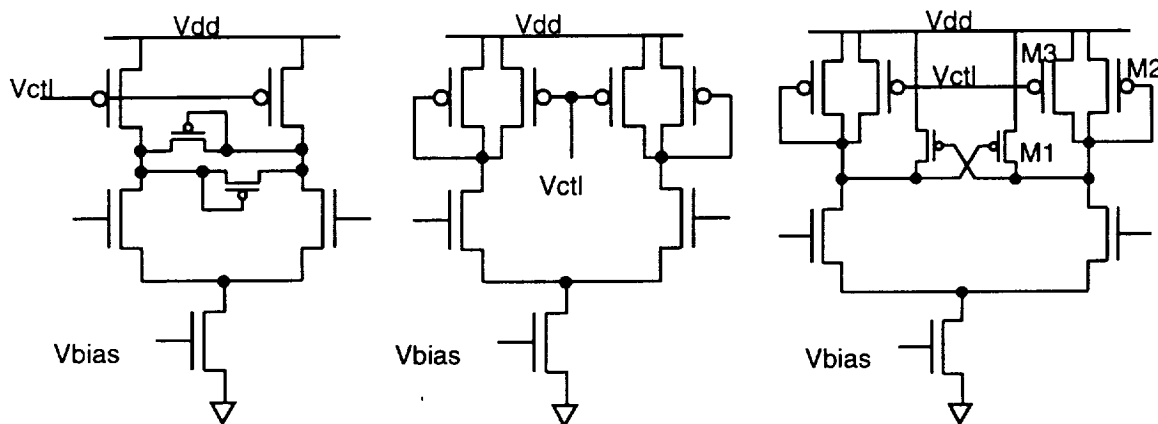

FIGURE 19. Differential delay buffer cells: (a) VCO_1, clamped-load; (b) VCO_2, symmetric load; (3) VCO_3, cross-coupled loads
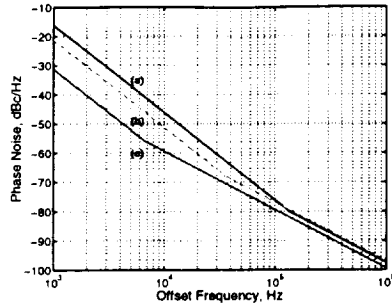
FIGURE 20. Predicted single-sideband phase noise: (a) VCO₁, (b) VCO₂, (3) VCO₃

Oscillator	$1/f^3$ corner	L{100KHz}
(a) Clamped Load	137KHz	-75dBc/Hz
(b) Symmetric Load	36KHz	-77dBc/Hz
(c) Cross-coupled Load	6.5KHz	-80dBc/Hz

TABLE 7. Theoretical phase noise and $1/f^3$ corner frequency for VCO₁, VCO₂, VCO₃

To study the trade-off between phase noise and power dissipation we plotted the power dissipation vs. frequency (figure 18) for differential pair devices of different widths W_n. The same figure also shows the corresponding $1/f^2$ phase noise bound using a frequency offset from the carrier of 100kHz. We assumed a typical 0.5µm CMOS process ($V_{dd}=3.3V$, $E_c=5.6x10^6V/m$, $f_{1/f}=3MHz$), $W_{pmos}=2W_n$, all minimum length ($L_{eff}=0.5µm$) short-channel devices, and $V_s= (V_{dd}-V_{ctl})$.

We observe that V_s increases with frequency, which increases the power dissipation, and lowers the phase noise. Still, the net effect on phase noise is an increase with frequency as predicted. For our design we selected the $W_n=6µm$ curve for an oscillation frequency of 200MHz at a power level of 2.1dBm (1.6mW @ 3.3V) with $L = -90dBc/Hz$ at 100KHz offset.

Differential Buffer Topology

Three ring oscillators were designed, each using a different load circuit for the delay buffer stage: VCO₁-clamped load, VCO₂-symmetric load, and VCO₃-cross-coupled load, respectively.

The clamped-load differential buffer (Figure 19a) used in VCO₁ has excellent noise and PSR characteristics [Horowitz93]. Symmetric load buffers (Figure 19b), as used in VCO₂, also have very good supply noise rejection characteristics and have been used extensively in PLL and clock generator designs [Maneatis96].

For the proposed cross-coupled load (Figure 19c, VCO₃), we started with a symmetric load stage with no cross-coupling and swept the width of the cross-coupling devices while maintaining the total width $(W_1+W_2=W_3=6µm)$ of the loads constant. The maximum symmetry of the output waveform was observed when the widths of M₁ and M₂ were equal to half the width of M₃.The cross-coupled diode loads clamp the output swing making the buffer delay insensitive to common-mode noise.

Results

To compare the three topologies, a more detailed noise analysis was performed. The predicted noise for a 4-stage oscillator in the $1/f^2$ region is given by:
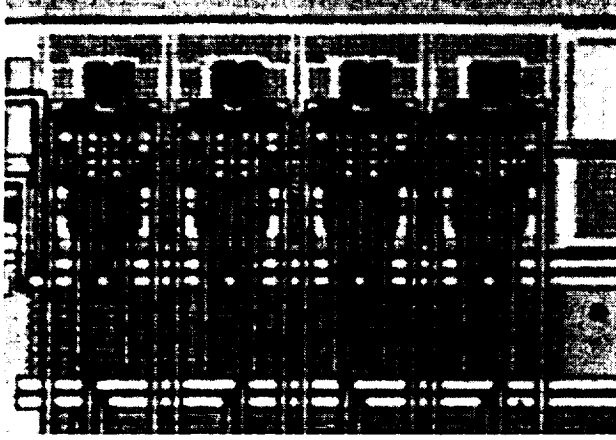
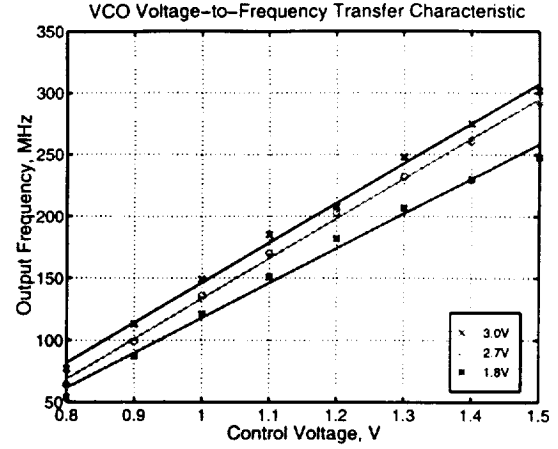**FIGURE 21.** Microphotograph of VCO_1 with 4 differential buffer delay stages

VCO Voltage-to-Frequency Transfer Characteristic

FIGURE 22. VCO_1 transfer characteristic

$$L\{\Delta f\} = \frac{\Gamma_{rms}^2}{(\pi V_s C_L \Delta f)^2} \cdot \frac{\overline{i_n^2}}{\Delta f}$$

where $\overline{i_n^2}/\Delta f$ is the total noise contribution from all sources at the output node. Figure 20 shows the predicted phase noise for VCO_1, VCO_2, and VCO_3. The $1/f^2$ regions are within 2.6dB of each other as it is to be expected for similarly sized noise sources. The model also predicts lower phase noise in the $1/f^3$ region for VCO_3 as it has better symmetry than the other two.

Table 7 shows the phase noise at 100KHz offset, and the $1/f^3$ corner frequency for all three oscillators running at 200MHz. Note that as expected due to the better symetry, the $1/f^3$ corner for VCO_3 is 95% lower than that of VCO_1. These theoretical phase noise and power vs. frequency characteristics are in good agreement with those reported previously [Betancourt97] for VCO_1.

A test chip was fabricated through MOSIS using the HP 0.5μm CMOS process (figure 21). The VCO_1 voltage-to-frequency transfer characteristics (K_v) was measured for different supply voltages (figure 22). Using an HP8590B Spectrum Analyzer, the phase noise was measured at -103.9dBc/Hz for a 500KHz offset which is very close to the predicted value of -103.2dBc/Hz. Test results using a more accurate phase noise measurement test set for VCO_1 are shown in figure 23 for operation at 150.9MHz, along with the phase noise predicted by the Hajimiri model. These measurements are within 2dB of the predicted values for frequency offsets between 10Hz and 1MHz, which is within the 2dB measurement accuracy of the RDL NTS-1000A instrument used.
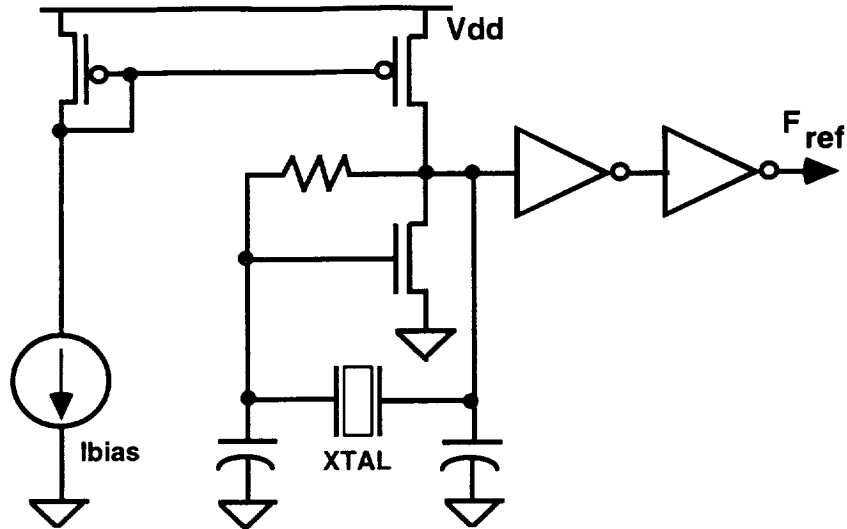
The BioLink Implantable Telemetry System

FIGURE 23. Pierce Crystal Oscillator Schematic Diagram

6.6 Crystal Oscillator Design

BioLink uses a low-power crystal oscillator design based on a Pierce topology (figure 23). A single transistor amplifier provides the negative resistance and a high-Q quartz crystal form the resonant circuit. Typical Q values for a quartz crystal exceed 10,000 making giving this oscillator excellent phase noise performance. Using a 24MHz crystal this circuit dissipates less than 150μA at 3V in a 0.5μm CMOS process. The size of the crystal is only 35mm^3 and does not affect the overall size of the implant.

6.7 Modulator Design

Figure 24 shows the block diagram of a typical QPSK transmitter. The incoming data bit stream is split into an in-phase and quadrature streams, for even and odd bits respectively. The two sequences are separately modulated by quadrature carriers. The two modulated signals, each of which can be considered a BPSK signal, are summed to produce the QPSK signal.

The encoder for the SS-DQPSK can be described by the diagram shown in figure 25. Here we overlayed the QPSK constellation with a state transition diagram that implements the differential π/2 phase encoding. We are guaranteed that only a +π/2 or -π/2 phase transitions occur at any given time. Only one of the modulators is active at a time, and if we rotate the QPSK constellation by π/2 then we can merge the multipliers into the single structure shown in figure 26. This circuit merges two VCO delay buffer cells, and adds inverting switches in order to generate all 4 phases.
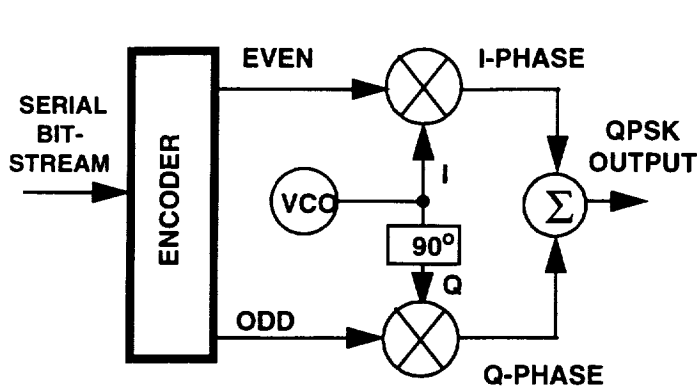
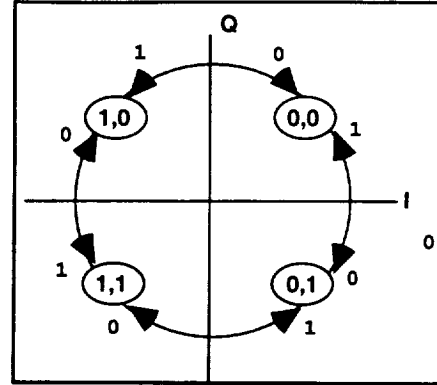**FIGURE 24.** Classic Quadrature Modulator Architecture

FIGURE 25. SS-DQPSK encoder state transition diagram

7.0 Super-regenerative Command Receiver

7.1 Principles of Super-regeneration

A simplified model of a superregeneration circuit is shown in Figure 27. Switch S_1 is periodically turned on and off so that the effective conductance between V_{tank} and Gnd alternates between positive and negative values. If the effective conductance across the tank is negative, V_{tank} grows exponentially. When S_1 turns off, then the amplitude decays. Oscillation is initiated either by the incoming signal or internal circuit noise. In real oscillators, there is always an amplitude limiting mechanism so that the oscillation amplitude eventually saturates.

The typical oscillation characteristic is shown in Figure 28. This superregenerative effect is best described by the following equation [Favre98]:

$$\Delta t = \tau \cdot \ln\left(\frac{A_1}{A_2}\right)$$

where Δt is time of advance, A_1 and A_2 are the amplitudes of the incident signal, and τ is a constant. The larger the input signal amplitude, the earlier does the oscillation start. Any amplitude modulation in the received carrier will produce a difference of areas under the oscillation envelope. An envelope detector is then used to recover the baseband signal.
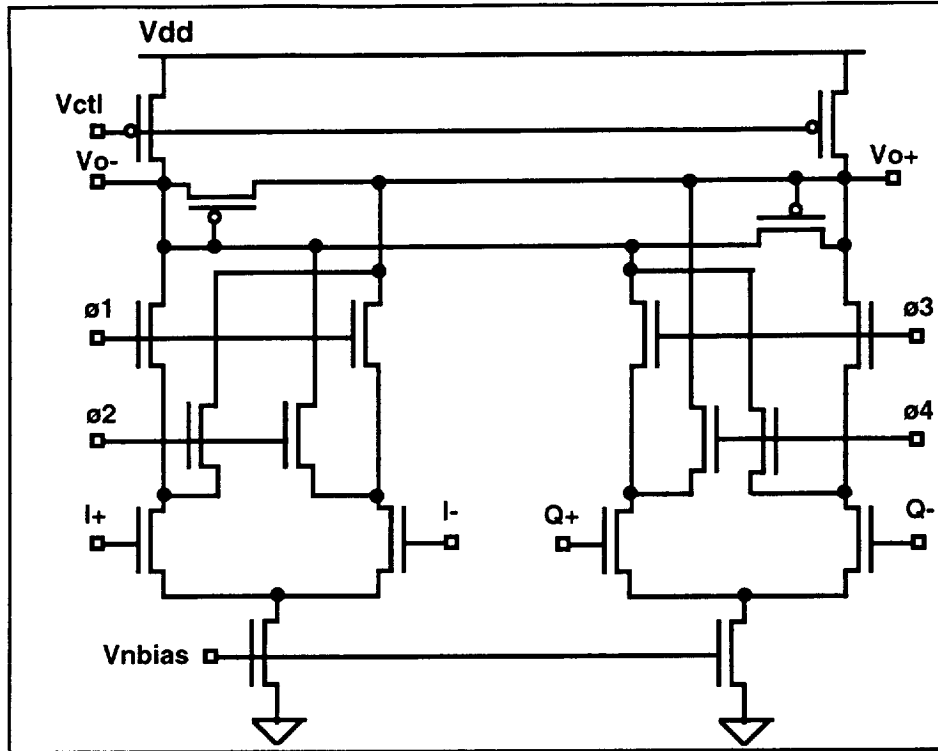
FIGURE 26. BioLink Quadrature Modulator Schematic

7.2 Receiver Architecture

The basic block diagram of a superregenerative AM receiver is shown in Figure 29. An isolation amplifier is necessary to prevent the oscillator from radiating back throught the antenna. The quenching network switches the effective resistance of the oscillator between positive and negative values. This causes the oscillation build up to be quenched out periodically. The quenching signal is critical to the performance of the superregenerative receiver. The optimal frequency for the quenching signal is given by the trade-off between sensitivity and gain. The best selectivity is obtained with a trapezoidal-shaped quenching signal[Armstrong22], [Fink38]. Also, smaller negative resistance and larger inductance help improve selectivity [Kalmus44]. Demodulation is performed by the subsequent rectifier and low pass filter (LPF).

The circuit schematic of the LC oscillator including the isolation amplifier and output buffer is shown in Figure 30. Transistors M1-M5 form the oscillator core. Cascode amplifier M6-M9 is needed to provide reverse isolation and prevents radiation of the carrier back to the antenna. The output of the oscillator is buffered by M10-M13. In the following sections we will describe the operation of these circuits.
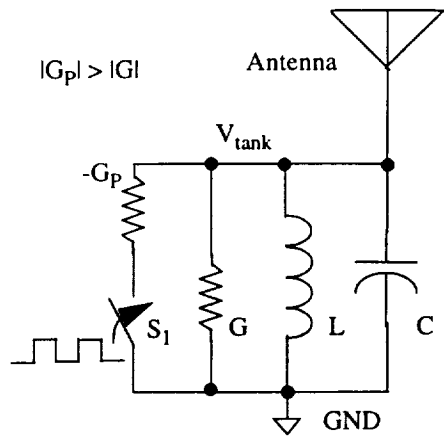
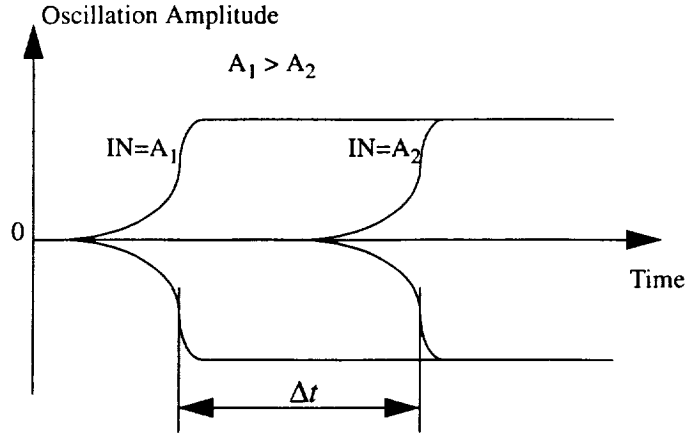**FIGURE 27. Simplified diagram of super-regeneration circuit**

FIGURE 28. Oscillation characteristic of super-regenerative receiver

7.3 Complementary Cross-Coupled LC Oscillator

The core of the superregenerative receiver is the oscillator. A complementary cross-coupled LC oscillator is preferred in high frequency applications due to its low phase noise, easy start-up and low power consumption [Ahrens97]. Cross-coupled transistors M1-M4 provide negative resistance across the parallel tank circuit through positive feedback. For oscillation to grow up, this negative conductance should be larger than the effective conductance across In_1 and In_2. The negative conductance G across the RLC tank is given by

$$G = -(g_{mN} + g_{mP})$$

The resonator consists of a surface-mount chip inductor, L, and tuning MOS capacitors C_{M1}, C_{M2}. The inductor is made by Murata [Murata96] and has a value of 56nH and a Q of 60 at 433MHz. A rather large value of inductance was chosen to minimize the influence of parasitics and process variation on the oscillation frequency. For a given Q, a larger inductor value reduces the power consumption since the effective parallel conductance across the tank becomes smaller. Once oscillation is initiated either by the input signal or by noise and enough positive feedback is sustained, the amplitude of oscillation will keep on growing, eventually saturating due to either a current-limiting or voltage-limiting mechanism [Hajimiri98]. In our design, the oscillator operates in the current-limiting regime so that the power consumption is well controlled by the tail current.

7.4 Isolation Amplifier and Output Buffer

The isolation amplifier (IA), M6-M9, a differential cascode is shown in figure 30. Simulations show that reverse isolation from In_1 and In_2 to Ant_1 and Ant_2 is 78.1dB. The voltage gain of the buffer is 0.7 with 6.6µA of bias. The output buffer, a differential source follower, consists of M10-M13.
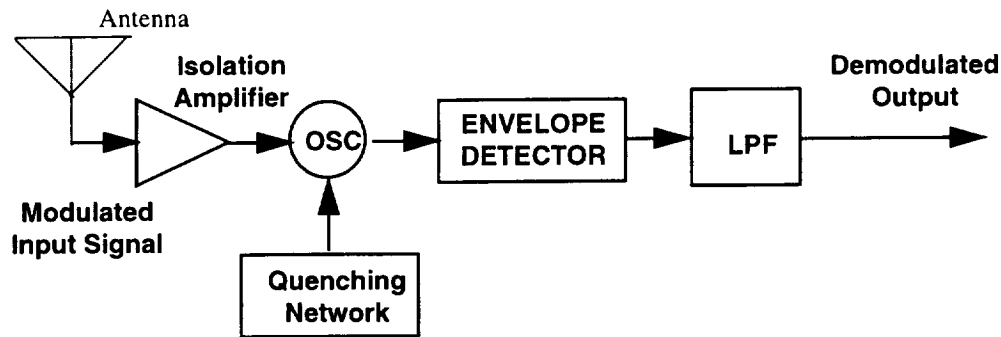
FIGURE 29. Block diagram of super-regenerative receiver

7.5 Envelope Detector: Rectifier and Low Pass Filter

The envelope detector is an absolute value circuit followed by a 4-pole low pass filter. Simulations show that the gain of the envelope detector is 1.6 with a supply current of 28.6μA.

An operational transconductance amplifier (OTA) and a level-shifter comprise one stage of the low pass filter. Both OTA and level shifter are loaded by capacitors, which provide two poles at 10kHz. The low pass filter consists of two stages, so that it provides a total of 4 poles at 10kHz.

7.6 Quenching Network

The quenching signal generator is implemented using a relaxation oscillator. It consists of a charge pump, a timing capacitor, and a Schmitt trigger. It produces rectangular pulse trains of 0.8V, 125kHz, and 50% duty cycle (typical). The W/L ratio of the transistors in the charge pump have been optimized to reduced power consumption. The charge pump biasing network uses two external resistors to set the pulse frequency and duty cycle. This adjustment also affects the sensitivity of the receiver since the quenching frequency and sensitivity are closely related as explained before.

7.7 Antenna Model

The antenna is a small copper loop etched on the transmitter's PCB. It is modeled as a series connected signal voltage source, a lumped inductor for the loop's inductance, and a resistor that accounts for losses due to resistance of the copper trace, skin effect and radiation resistance. Simulation shows that the impedance seen from the Ant$_1$ and Ant$_2$ nodes into the isolation amplifier is 11.68kΩ - j1.11kΩ By using capacitive tapping, a good input match is easily achieved. With the proper antenna model, a S$_{11}$ of -26dB was simulated.
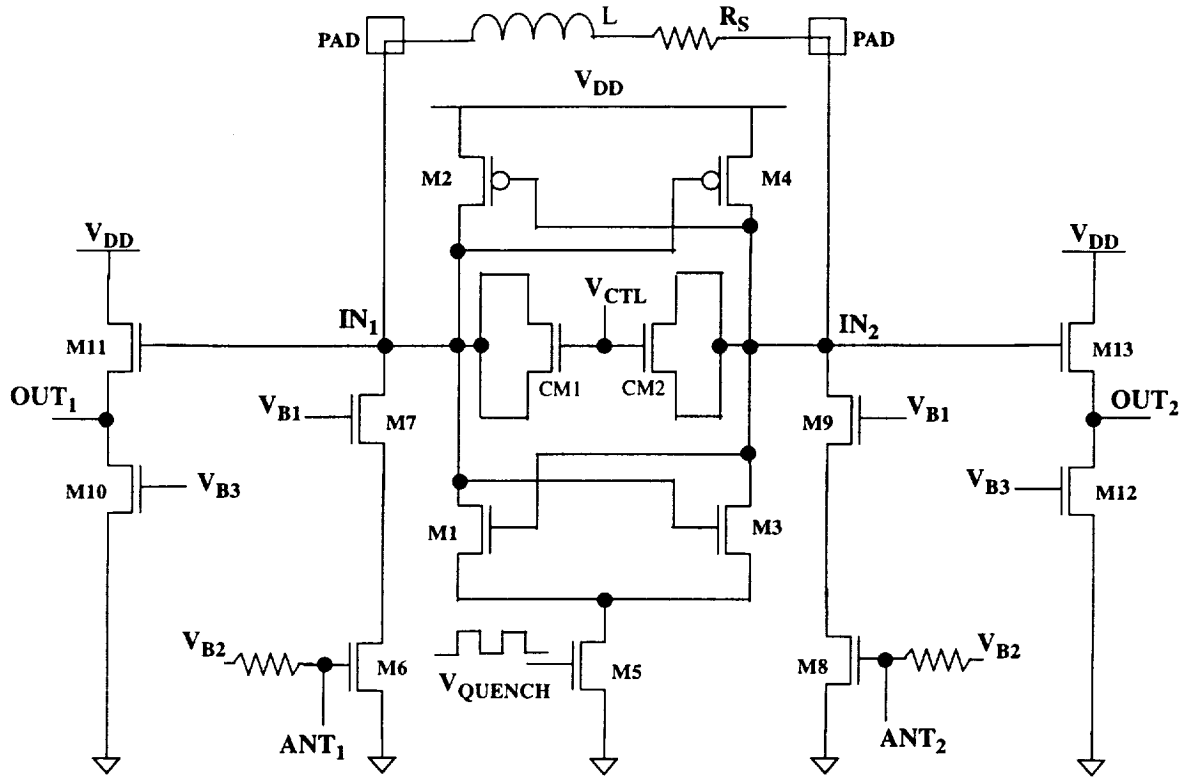
FIGURE 30. Schematic of LC oscillator, isolation amplifier, and output buffer

7.8 Simulation Results

A $10\mu V$, 5kHz, and 50% duty cycle ASK signal was applied to the antenna inputs. A summary of the achieved specifications (simulations) is given in Table 8.

7.9 Conclusion

A superregenerative AM receiver designed on $0.5\mu m$ CMOS technology was demonstrated. An average supply current of $100.2\mu A$ with 3.0V supply voltage was achieved with performance comparable to previously reported work in a bipolar technology [Farve98]. With $300\mu W$, average power dissipation, this receiver is suitable for low-power biotelemetry applications.

Supply Voltage	3.3V
Supply Current (avg)	$100\mu A$
Oscillation Frequency	433MHz
Quench Frequency	125kHz
S_{11}	-26.24dB
LPF cutoff frequency	10kHz
Max. Data Rate	125kHz

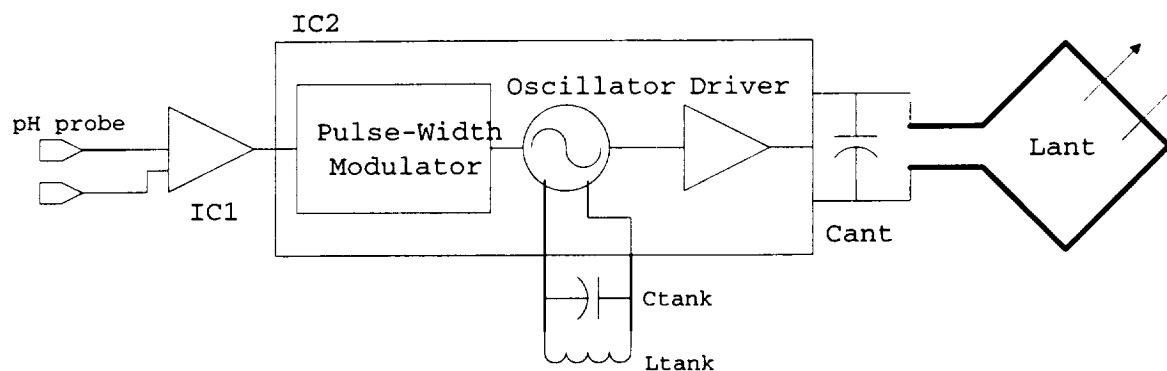**TABLE 8. Summary of simulated results for Super-regenerative receiver**

FIGURE 31. Block diagram of pH Analog Data Module and Biotelemetry Transmitter

8.0 A pH Analog Data Module

A block diagram for a pH Analog Data Module is shown in figure 31. It consists of the NASA-developed pH sensor, a high impedance buffer amplifier, a pulse width modulator, a differential LC voltage-controlled oscillator, and an antenna driver. The mV-level pH signal from the high-impedance electrode controls a Pulse Width Modulator (PWM) whose duty cycle changes with the input voltage level.

8.1 pH Sensor

A pH sensor based on a dual-lumen catheter has been developed and tested in animal models [Hines96]. The pH sensor is based on a polymeric H+ ionophore (Tri-n-dodecylamine) neutral carrier membrane cast around the tip of a microbore PVC catheter. Baseline drift is on the order of 4mV every 24 hours. Sensor sensitivity is in the range of 57-60mV/pH unit at room temperatures (theoretical slope is 59mV/pH @ 25C), and sensitivity loss is 2% over a 12 day period. The physiologically significant range of interest (6.8-8.0pH) falls within the linear range of the sensor, with response time less than 3 seconds.

8.2 Signal Conditioning and A/D Converter

The biologically significant range is 6 to 8.5pH units which corresponds to a ±50mV signal from the pH sensor. We designed the system for ±200mV differential input to accommodate the expected physiological response, baseline drift, and systematic offsets. The mV level pH signal from the high-impedance electrode is buffered by U1, a Max406 low-noise opamp that is configured with unity gain and 8KHz 3-dB bandwidth. We take advantage of the dominant pole of the amplifier to low-pass filter the signal before further processing.

The next block is a Pulse Width Modulator (PWM) that consists of a 100Hz-relaxation oscillator whose duty cycle varies with a control voltage. For the total input voltage range of 400mV, and 10ms nominal period, the "gain" of the PWM can be defined by

$$dc = 0.5 + \Delta V_i$$

where dc is the duty cycle of the oscillator and ΔV_i is the differential input voltage.

The circuitry for the PWM is shown in Figure 32. It consists of an input differential stage that steers the currents I_1 and I_2 through mirrors into a charge pump circuit. The total current I_{ref} is kept constant by the current reference shown in Figure 33.

Transistors M2 and M3 form an input differential pair, biased by M1. The gate lengths of M2 and M3 are 50 times the minimum to linearize their transconductance. The differential pair converts the pH voltage signal into a differential current. Current I_1 is directed into M8 and M9, where diode connected M7 equalizes V_{ds} on M6 and M8, forming a modified Wilson current mirror. Similarly current I_2 (from M5 and M4) is mirrored to M11 and M12. Devices M13, M14, M16 and M17 set the current on M15. M10 sets the sink current for the charge pump on M20, and M15 sets the source current on M19.

The oscillator consists of a charge pump made up by current sources M19, M20 and switches M18, M21, a schmitt trigger U1, an inverter U2, and a timing capacitor C1. The output of the pump is integrated by capacitor C1 whose voltage serves as the input to the schmitt trigger. U1 is sized to have 1-volt of hysteresis, ΔV. When U1's output is high, inverter U2 switches M18 on and the capacitor voltage ramps up as it is being charged by current I_1 from M19. When the capacitor voltage exceeds the schmitt trigger threshold, U1 goes low turning on
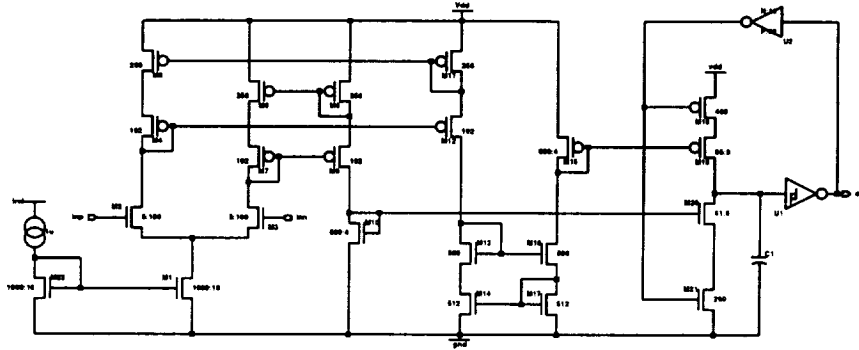

FIGURE 32. Schematic for Pulse Width Modulator

M21 and discharging the capacitor at a rate determined by the current I_2 set by M20. The charge and discharge times of the capacitor can be approximated by

$$t_c = \frac{q_{max}}{kI_1}, t_d = \frac{q_{max}}{kI_2}$$

and the oscillation frequency is given by

$$f = \frac{1}{t_c + t_d} = \frac{kI_1 \cdot I_2}{4q_{max}I_{ref}}$$

where I_{ref} is a constant $1\mu A$, , and k is the scaling factor of the current mirrors, which is set to 1/33. The frequency can also be expressed in terms of the input voltage ΔV_i if we assume that the transconductance is linear over the input range of ΔV_i. The currents I_1 and I_2 can then be expressed by

FIGURE 33. Simplified diagram for Current Reference

$$I_1 = \frac{I_{ref} + \Delta I}{2}$$

$$I_2 = \frac{I_{ref} - \Delta I}{2}$$

where $\quad I_1 - I_2 = \Delta I = g_m \Delta V_i$

This is true for

$$\Delta V_i \leq \sqrt{\frac{2I_{ref}}{\mu_n C_{ox}(W/L)_{2,3}}} \cong 500mV$$

where $\mu_n C_{ox} = 154\mu A/V^2, q_{max} = C_1 \cdot \Delta V$, and the differential pair aspect ratio, $(W/L)_{2,3}$ is 5/100 in our design. Using the expression for transconductance of long-channel devices in saturation,
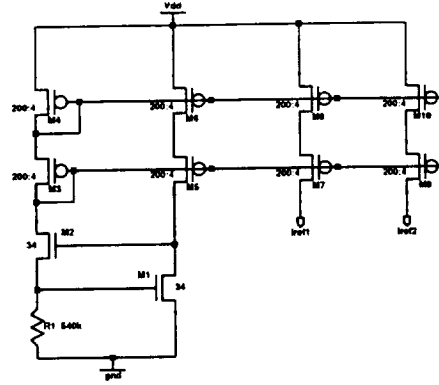
$$g_m = \sqrt{\mu_n C_{ox}(W/L)_{2,3} I_{ref}}$$

we arrive at the following expression for the frequency:

$$f = \frac{kI_{ref}}{4q_{max}} \left[1 - \mu_n C_{ox} (W/L)_1 \cdot \Delta V_i^2\right]$$

Simulations (figure 34) show a parabolic response with respect to the input voltage ΔV_i, as predicted.

A differential voltage at the inputs of M2 and M3 varies the ratio of I_1 and I_2, changing the duty cycle of the output waveform. The duty cycle is given by

$$dc = \frac{t_c}{t_c + t_d} = \frac{I_2}{I_{ref}} = \frac{1}{2} - \frac{\Delta I}{2I_{ref}} = \frac{1}{2} - \frac{g_m}{2I_{ref}} \Delta V_i$$

Observe that to the first order the duty cycle insensitive to variations in Vdd, C, or ΔV. We simulated the operation of the PWM and observed that it has good linearity over the range of interest (± 100mV). The duty cycle varies from 66% down to 33% duty cycle (figure 35). Power supply rejection is very good: for a 20% change in Vdd, the duty cycle varied less than 1.5%. The sensitivity of frequency with Vdd can be attributed to changes of the reference I_{ref} with Vdd.
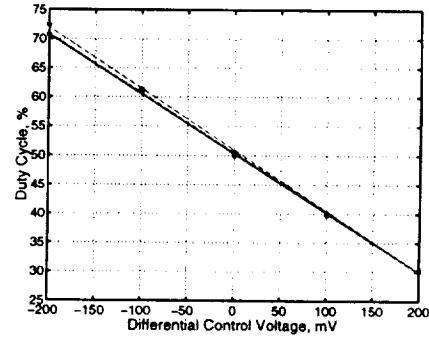
FIGURE 34. Simulated duty cycle vs. input voltage of PWM: (*) Vdd=3.3V, (x) Vdd=3.0V, (o) Vdd=2.7V

8.3 Current Reference Circuit

The bias reference used by the PWM oscillator is shown in figure 33. The double cascode formed by M3, M4, M5 and M6 force the same current through M1 as that through R_1. Then,

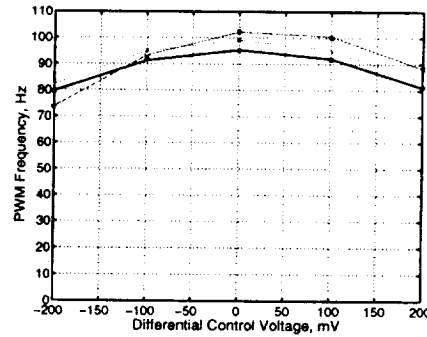$$I_{ref} \cdot R_1 = V_{tn} + \sqrt{\frac{2I_{ref}}{\mu_n C_{ox}(W/L)_1}}$$

FIGURE 35. Simulated Frequency vs. input voltage o PWM: (*) Vdd=3.3V, (x) Vdd=3.0V, (o) Vdd=2.7V

The BioLink Implantable Telemetry System

where V_{tn} is M1's threshold voltage (we have neglected channel length modulation and body effect). By proper sizing of M1 we can make the second term of the equation small compared to V_{tn}, and the current I_{ref} is given approximately by

$$I_{ref} = \frac{V_{tn}}{R1}$$

A feedback circuit made up by M2 regulates the current. If the current through M1 rises, the voltage at the gate of M2 drops and reduces the output current, which is mirrored to M1. Transistors M9 and M10 provide a reference for the PWM.

8.4 Results

The pH biotelemeter was fabricated through the MOSIS service as a single chip using the HP-0.5μm CMOS process. Figure 36 shows a microphotograph of the chip. It has an area of 1mm². The pH analog circuit consumes less than 5μA at 3.3V.
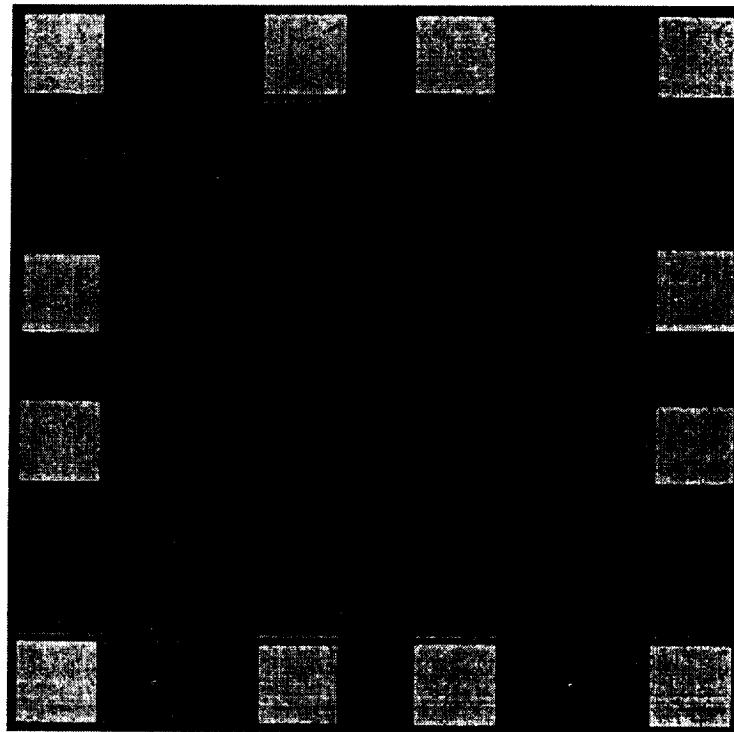

FIGURE 36. Microphotograph of pH biotelemetry chip

9.0 Conclusions

A low-power biotelemeter suitable for chronic sensor implant studies is being developed. It implements a frequency synthesizer based on the FLL architecture just described. The FLL synthesizer does not require a frequency divider with its associated power dissipation, but it imposes more stringent phase noise requirements on the VCO. To minimize power consumption of the VCO, a design technique using the Hajimiri phase noise model was presented. Measurements of phase noise show good agreement with the theory.

A system architecture based on a Frequency-Locked Loop (PLL) Frequency Synthesizer was defined and a novel self-synchronizing phase modulation scheme suitable for low power implementation was deviced. A full system-level simulation of the PLL was performed and loop filter parameters were determined. The implantable antenna has been designed, simulated and constructed. An implant package compatible with the ABTS requirements is also proposed.

We also propose a novel superregenerative receiver architecture for implementing the command receiver. The superregenerative receiver's simplicity, low cost, and low power consumption has made it the receiver of choice for short-distance data communications, remote control and home automation We present the design of a super-regenerative AM receiver implemented in a 0.5μm CMOS technology that operates at 433.92MHz and dissipates only 300μW.

Further work entails detailed transistor-level design of the FLL and superregenerative receiver and a monolithic implementation of an implantable transceiver in 0.5μm CMOS technology.

10.0 Acknowledgments

11.0 References:

[Ahrens97] T. I. Ahrens, A. Hajimiri and T.H. Lee, "A 1.6GHz 0.5mW CMOS LC Low Phase Noise VCO Using Bond Wire Inductance," *First International Workshop on Design of Mixed-Mode Integrated Circuits and Applications*, Cancún, Mexico, Jul. 1997, pp. 69-71.

[Allstot93] D.J. Allstot, et al., "Folded Source-Coupled Logic vs. CMOS Static Logic for Low-Noise Mixed-Signal ICs", IEEE Journal of Solid-State Circuits, vol. 40, no. 9, pp. 553-563, Sept. 1993.

[Armstrong22] E. H. Armstrong, "Some Recent Developments of Regenerative Circuits," *Proceedings of the I.R.E.*, Aug. 1922, pp. 244-260.

[Batty85] J.R. Batty, "Implant communication system with frequency shift means.", U.S. Patent No. 4,532,932, Aug. 6, 1985.

[Bazuin89] B.J. Bazuin, "Totally-implantable biomedical dimension-telemetry.", Ph.D. Dissertation, Stanford University, 1989.

[Betancourt97] R.J. Betancourt-Zamora, A. Hajimiri, and T.H. Lee, *"A 1.5mW, 200MHz CMOS VCO for wireless biotelemetry,"* First International Workshop on Design of Mixed-Mode Integrated Circuits and Applications, Cancun, Mexico, pp. 72-74, July, 1997.

[Black53] Harold S. Black, "Modulation Theory", D. Van Nostrand Co., 1953, pp. 263-298.

[Crawford94] J.A.Crawford, "Frequency Synthesizer Design Handbook", Artech House, Boston, 1994.

[Cupal89] J.J. Cupal, R.W. Weeks, "Digital encoding techniques for the telemetering of biological data." Biotelemetry X, Proc. Int'l Symp. on Biotelemetry, pp. 39-50, University of Arkansas Press, 1989.

[Dorman85] M.G. Dorman, "An IC-based telemetry system for neurophysiology." Ph.D. Dissertation, Stanford University, 1985.

[Eichenberger89] C. Eichenberger, W. Guggenbühl, "Dummy Transistor Compensation of Analog MOS Switches.", IEEE Journal of Solid-State Circuits, vol. 24, no. 4, pp. 1143-1146, Aug. 1989.

[Farve98] P. Farve, Norbert Joehl, Michel Declercq, Catherine Dehollain, and Philippe Deval, "A 2V, 600μA, 1GHz, BiCMOS Superregenerative Receiver," *ISSCC Digest of Technical Papers*, San Francisco, Calif., Feb. 1998, pp. 128-129.

[FCC15] FCC rules and regulations , part 15

[Fernald92] K.W. Fernald, et al., "A self-tuning digital telemetry IC for use in a microprocessor-based implantable instrument.", IEEE Journal of Solid-State Circuits, vol. 27, no. 12, pp. 1826-1832, Dec. 1992.

[Fink38] F. W. Frink, "The Basic Principles of Superregenerative Reception," *Proceedings of the I.R.E.*, Jan. 1938, pp. 76-106.

[Fotowat84] A. Fotowat-Ahmady, et al., "RF Attenuation of an Implantable Transmitter Signal", IEEE Eng. in Med. and Biol. 6th Conference, pp.738-741, Sept. 1984.

[Fotowat91] A. Fotowat-Ahmady, "RF transmission and micropower filtering circuits for implantable ultrasonic blood flow telemetry.", Ph.D. Dissertation, Stanford University, 1991.

[Fryer74] T.B. Fryer, R.M. Westbrook, "A multichannel biotelemetry transmitter utilizing a PCM subcarrier.", Biotelemetry II, Proc. Int'l Symp. on Biotelemetry, pp. 202-204, S. Karger, 1974.

[Fujimoto87] K. Fujimoto, A. Henderson, et al., "Small Antennas", John Wiley & Sons, 1987.

[Gardner80] F. M. Gardner, "Charge Pump Phase-Lock Loops", IEEE Trans. Comm., vol. COM-28, Nov. 1980, pp. 1849-1858.

[Geisler95] M.S. Geisler, "A Microcontroller Based PCM Biotransceiver System for the ABTS (Advanced Biotelemetry System)", NASA-Ames Final Report, August 1995.

[Hajimiri98a] A. Hajimiri and T.H. Lee, "A general theory of phase noise in electrical oscillators," IEEE Journal of Solid-State Circuits, vol. 33, pp. 179-194, February 1998.

[Hajimiri98b] A. Hajimiri and T.H. Lee, "Phase noise in multi-gigahertz CMOS ring oscillators," Custom Integrated Circuits Conference Digest, pp. 49-52, May 1998.

[Hajimiri98c] A. Hajimiri and T.H. Lee, Correction to "A general theory of phase noise in electrical oscillators," IEEE Journal of Solid-State Circuits, vol. 33, p. 928, June 1998.

[Hajimiri98d] A. Hajimiri and T.H. Lee, "Phase Noise in CMOS Differential LC Oscillators," Symposium on VLSI circuits, Honolulu, Hawaii, Jun. 1998, pp. 48-51.

[Hardy79] James Hardy, "High Frequency Circuit Design", Prentice Hall, 1979, pp. 288-290.

[Henry92] D.A. Henry, "Synchronous telemetry system and method for an implantable medical device", U.S. Patent No. 5,137,022, Aug. 11, 1992.

[Hickman93] I. Hickman, "Newnws Practical RF Handbook", Butterworth-Heinemann Ltd., Oxford, England, 1993.

[Hines95] J.W. Hines, C.J. Somps, et al., "Advanced Biotelemetry Systems for Space Life Sciences: pH Telemetry," 13th International Symposium on Biotelemetry, Williamsburg, Virginia, March 1995, p. 37.

[Hines96] J.W. Hines, C.J. Somps, et al., "Telemetric Sensors for the Space Life Sciences", 18th Annual IEEE Engineering in Medicine and Biology Conference, Amsterdam, Oct. 1996, pp.30-31.

[Horowitz93] M. Horowitz, et al., "PLL design for a 500MB/s interface," Int'l Solid-State Circuits Conference Digest, pp. 160-161, February 1993.

[Jefferson86] Jefferson Laboratories, Inc. "Report on Biotelemetry Antenna Development", August 1996.

[Jeutter83] D.C. Jeutter, "Overview of biomedical telemetry techniques.", IEEE Eng. in Med. and Biol. Magazine, pp.17-24, March 1983.

[Jeutter95] D.C. Jeutter, J.W. Hines, M.S. Geisler, "Microcontroller Based PCM Bio-Transceiver System for the ABTS (Advanced Biotelemetry System)", Proc. Amer. Inst.. Aero. & Astro., 1995.

[Ji92] J. Ji, K.D. Wise, "An implantable CMOS circuit interface for multiplexed microelectrode recording arrays." IEEE Trans. Biomed. Eng., vol. 27, no. 3, pp. 433-443, March 1992.

[Kalmus44] H. P. Kalmus, "Some Notes on Superregeneration with Particular Emphasis on Its Possibilities for Frequency Modulation," *Proceedings of the I.R.E.*, Oct. 1944, pp. 591-600.

[Knutti83] J.W. Knutti, et al., "Integrated circuit implantable telemetry systems.", IEEE Eng. in Med. and Biol. Magazine, pp.47-50, March 1983.

[Ko80] W.H. Ko, "RF-powered cage system for implant biotelemetry.", IEEE Trans. Biomed. Eng., vol. 27, no. 8, pp. 460-467, Aug. 1980.

[Lau95] H. Lau, "Performance concerns guide the design of pager antennas", Microwaves & RF, December 1995, pp. 95-106.

[Leung86] A.M. Leung, et al., "Intracranial pressure telemetry system using semicustom integrated circuits.", IEEE Trans. Biomed. Eng., vol. 33, no. 4, pp. 386-395, April 1986.

[Li84] P.W. Li, et al., "A ratio-independent algorithmic analog-to-digital conversion technique.", IEEE Journal of Solid-State Circuits, vol. SC-19, no. 6, pp. 828-836, Dec. 1984.

[Linden95] D. Linden, "Handbook of Batteries", McGraw-Hill 1995.

[Mackay70] R.S. Mackay, "Bio-medical telemetry: sensing and transmitting biological information from animals and man", John Wiley & Sons, 1970.

[Maneatis93] J. Maneatis and M. Horowitz, *"Precise delay generation using coupled oscillators,"* IEEE Journal of Solid-State Circuits, vol. 28, pp. 1273-1282, December 1993.

[Maneatis96] J. Maneatis, *"Low-jitter and process-independent DLL and PLL based on self-biased techniques,"* Int'l Solid-State Circuits Conference Digest, pp. 130-131, 430, February 1996.

[McCutcheon76]. E.P. McCutcheon, et. al, "An inductively powered implantable multichannel telemetry system for cardiovascular data.", Biotelemetry III, Proc. Int'l Symp. on Biotelemetry, pp. 71-74, Academic Press, 1976.

[McCreary75] J.L. McCreary, P.R. Gray, "All-MOS charge redistribution analog-to-digital conversion techniques." ,IEEE Journal of Solid-State Circuits, vol. SC-10, no. 6, pp. 371-379, Dec. 1975.

[Messerschmitt79] D. G. Messerschmitt, "Frequency Detector for PLL Acquisition in Timing Recovery", IEEE Trans. Comm., vol. COM-27, Sep. 1979, pp. 1288-95.

[Murata96] "LQN1A Series Surface Mount Inductors," *EMI Filter/Chip Inductor Catalog No. E-06-D*, Murata Electronics, 1996, p. 39.

[NASA95] Life Sciences Advanced BioTelemetry System (LS-ABTS) Engineering Specification, NASA-Ames Research Center, January 11, 1995.

[NASA96] "Monitoring the Mysteries of the Fetus", NASA-Ames Research Center, Videotape 1996

[Neukomm76] P.A. Neukomm, "Health hazards for telemetry RF exposure? A review on the interactions between electromagnetic fields and biosystems", Biotelemetry III, Proc. Int'l Symp. on Biotelemetry, pp. 41-44, Academic Press, 1976.

[Neukomm89] P.A. Neukomm, et al. "Passive telemetry by absorption modulation." Biotelemetry X, Proc. Int'l Symp. on Biotelemetry, pp. 39-50, University of Arkansas Press, 1989.

[Owens86] B.B. Owens, Ed. ,"Batteries for implantable biomedical devices.", Plenum Press, 1986.

[Santic82] A. Santic, et al., "Micropower electronic switches for implanted instrumentation.", IEEE Trans. Biomed. Eng., vol. 29, no. 8, pp. 583-589, Aug. 1982.

[Schild89] J.H. Schild, et al., "A multichannel implantable telemeter for acquisition of physiological data." Biotelemetry X, Proc. Int'l Symp. on Biotelemetry, pp. 39-50, University of Arkansas Press, 1989.

[Schulman80] J.H. Schulman, et al., "Telemetry means for tissue stimulator system.", U.S. Patent No. 4,223,679, Sep. 23, 1980.

[Schwartz80] Mischa Schwartz, "Information transmission, modulation and noise", McGraw-Hill, 1980, pp. 212-231.

[Shannon49] C.E. Shannon, "Communication in the Presence of Noise.", Proc. IRE, vol. 37, pp. 10-21, January 1949.

[Shapiro89] F.B. Shapiro, "An integrated circuit for biotelemetry with digital IC sensors", Ph.D. Dissertation, Stanford University, 1989.

11.0 References:

[Shih86] C.C. Shih, P.R. Gray, "Reference refreshing cyclic analog-todigital and digital-to-analog converters." ,IEEE Journal of Solid-State Circuits, vol. SC-21, no. 4, pp. 544-554, Aug. 1986.

[Silvian93] S. Silvian, "High speed reflected impedance telemetry system for implantable medical device.", U.S. Patent No. 5,264,843, Nov. 23, 1993.

[Slocum85] C.D. Slocum, V.T. Cutolo, "Analog telemetry system for biomedical implant", U.S. Patent No. 4,543,953, Oct. 1, 1985.

[Smith72] G.S. Smith, "Proximity Effect in Systems of Parallel Conductors", Journal of Applied Physics, May 1972, pp. 2196-2203.

[Smith93] D.R. Smith, "Digital Transmission Systems, 2nd Ed.", Van Nostrand Reinhold, 1993.

[Somps94], Chris Somps, NASA-Ames Research Center, personal communication.

[Somps95], Chris Somps, NASA-Ames Research Center, personal communication.

[Song87] Bang-Sup Song, "A Narrow-Band CMOS FM Receiver Based on Single-Sideband Modulation IF Filtering", IEEE Journal of Solid-State Circuits, vol. SC-22, no. 6, pp. 1147-1154, Dec. 1987.

[Stallings85] W. Stallings, "Data and Computer Communications", Macmillan Publishing Co., 1985.

[Terman50] F.E. Terman, Radio Engineers' Handbook, McGraw Hill, 1950.

[Towe86] B.C. Towe, "Passive biotelemetry by frequency keying", IEEE Trans. Biomed. Eng., vol. 33, no. 10, pp. 905-909, Oct. 1986

[vonKaenel96] V. von Kaenel, D. Aebischer, C. Piguet, and E. Dijkstra. A 320MHz, 1.5mW @ 1.35 V CMOS PLL for microprocessor clock generation. IEEE JSSC 31, 11 (1996), 1715-1722.

[Wegmann87] George Wegmann, et al., "Charge Injection in Analog MOS Switches.", IEEE Journal of Solid-State Circuits, vol. SC-22, no. 6, pp. 1091-1097, Dec. 1987.

[Withers91] D.J. Withers, "Radio Spectrum Management.", Peter Peregrinus Ltd., 1991.

[Yee79] Y.S. Yee, et al., "A two-stage weighted capacitor network for D/A-A/D conversion.", IEEE Journal of Solid-State Circuits, vol. SC-14, no. 4, pp. 778-781, Aug. 1979.